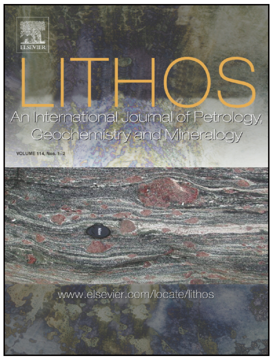

Assessment of magmatic versus post-magmatic processes in the Mueilha rare-metal granite, Eastern Desert of Egypt, Arabian-Nubian Shield

Amany M.A. Seddik, Mahmoud H. Darwish, Mokhles K. Azer, Paul D. Asimow

PII: S0024-4937(20)30180-8

DOI: https://doi.org/10.1016/j.lithos.2020.105542

Reference: LITHOS 105542

To appear in: *LITHOS*

Received date: 2 March 2020

Revised date: 15 April 2020

Accepted date: 15 April 2020

Please cite this article as: A.M.A. Seddik, M.H. Darwish, M.K. Azer, et al., Assessment of magmatic versus post-magmatic processes in the Mueilha rare-metal granite, Eastern Desert of Egypt, Arabian-Nubian Shield, *LITHOS* (2020), https://doi.org/10.1016/j.lithos.2020.105542

Assessment of magmatic versus post-magmatic processes in the Mueilha rare-metal granite, Eastern Desert of Egypt, Arabian-Nubian Shield

***Amany M. A. Seddik*[a]*, Mahmoud H. Darwish*[a]*, Mokhles K. Azer*[b1]*, Paul D. Asimow*[c]**

[a]Geology Department, Faculty of Science, New Valley University, El-Kharga, 72511 Egypt

[b]Geological Sciences Department, National Research Centre, Cairo, Egypt

[c]Division of Geological & Planetary Sciences, California Institute of Technology, Pasadena CA 91125 USA

---

[1] **Corresponding Author:** Prof. Mokhles K. Azer (mokhles72@yahoo.com)

Abstract

The Mueilha rare-metal granite, exposed in the central Eastern Desert of Egypt, is a post-collisional intrusion that formed in the final magmatic stage of the evolution of the Arabian-Nubian Shield. The Mueilha intrusion was emplaced as a high-level magmatic cupola into metamorphic country rocks. It consists of two cogenetic intrusive bodies: an early phase emplaced at shallow depth and now penetratively altered to white albite granite and a later phase of red granites emplaced at greater depth that better preserve magmatic features. The albite granite is less common and represents the upper margin of the Mueilha intrusion, the apex of the magmatic cupola. The red granites are volumetrically dominant and appears to have crystallized from the margins inward, forming a composite pluton zoned from muscovite granite to alkali feldspar granite. All parts of the Mueilha pluton appear to have been emplaced within a short time interval, before complete crystallization of the earliest phase. The geochemistry of the Mueilha granites is typical of rare-metal granites, characterized by high SiO_2, Na_2O+K_2O, Nb, Rb, Ta, Y, U, Th, Sn, and W with depletion in P, Mg, Ti, Sr and Ba. They are weakly peraluminous and highly fractionated with A-type character. The chondrite-normalized REE patterns have strongly negative Eu anomalies, typical of highly differentiated granites that evolved through a transitional magmatic–hydrothermal stage. The primary magma feeding the Mueilha intrusion was generated by partial melting of the juvenile crust of the Arabian-Nubian Shield; it subsequently underwent extensive fractional crystallization and metasomatism by late- to post-magmatic fluids. Separation of fluids from the oversaturated melt promoted both diffuse greisenization and focused segregation of pegmatite and fluorite and quartz veins. Alkalis liberated from feldspars consumed by greisenization were redeposited during albitization in the uppermost part of the magma chamber. Despite penetration of the intrusion boundary by discrete dikes, veins, and aphophyses, diffuse alteration of the metamorphic country rocks is not apparent. Primary columbite-series minerals crystallized from the melt and were later partly replaced by secondary Nb and Ta minerals (fluorcalciomicrolite and wodginite) during hydrothermal alteration.

Keywords: Arabian-Nubian Shield, highly fractionated granite, Nb–Ta oxide minerals, Magmatic–hydrothermal evolution

1. Introduction

The Precambrian basement rocks of the Nubian Shield are exposed in the Eastern Desert of Egypt, NE Sudan, Somalia, and Ethiopia. Until the opening of the Red Sea less than 30 Ma ago, the Nubian and Arabian Shields were contiguous parts of the Arabian-Nubian Shield (ANS). The ANS represents the most juvenile continental crust on the Earth (Stoeser and Frost, 2006). It developed in Neoproterozoic time (850-590 Ma) during the Pan-African orogeny (Stern, 1994). There were a series of major orogenic events through which continental, island arc, and oceanic terranes collided and amalgamated between East and West Gondwana, which then collided to form the crystalline basement of the Gondwana supercontinent. Later, widespread post-collisional granitoid intrusions and their volcanic equivalents were emplaced into the juvenile upper crust of the Shield.

The Eastern Desert of Egypt is intruded by voluminous granitoids of various ages, geochemical characteristics and tectonic regimes (e.g. El-Sayed et al., 2002; Farahat et al., 2007; Azer et al., 2019). One of the most striking features of these granitoids is the abundance of post-collisional granitic intrusions, many of them enriched in rare metals (e.g. Helba et al., 1997; Abu El-Rus et al., 2017; Sami et al. 2017, 2018; Azer et al., 2019; Heikal et al., 2019, Abuamarah et al., 2019). The rare-metal granites of the Eastern Desert have received much attention from economic geologists due to their substantial potential as sources of Nb, Ta, rare earth elements (REE), U, Zr and Th (e.g. Helba et al., 1997; Abou El Maaty and Ali Bik, 2000; Abuamarah et al., 2019; Azer et al., 2019; Heikal et al., 2019). Despite numerous studies and widespread outcrops in the Eastern Desert, however, considerable controversy about their origin and geotectonic evolution still remains.

The Mueilha intrusion (Fig. 1c), the target of the present work, is one of the most outstanding examples of rare-metal (Ta-Sn-Nb) granite in the Eastern Desert. The published literature concerning the Mueilha intrusion is sparse and contradictory (e.g. Salem et al., 1985; Morsy and Mohamed, 1992; Hassanen et al., 1995; Abou El Maaty and Ali Bik, 2000; Mohamed, 2013; El-Galy et al., 2016; Abu El-Rus et al., 2017). Various authors have adopted models of the origin of the intrusion ranging from entirely metasomatic to entirely magmatic, as well as hybrids of these, but no unique petrogenetic model has been proposed that satisfactorily explains the features of the intrusion. This work integrates field observations, petrography, mineral chemistry and whole-rock chemical analyses to examine the petrological characteristics of the Mueilha rare-metal granites in order to distinguish between magmatic and metasomatic stages in the evolution of the pluton. Both stages are required. We also aim to better document and understand the alteration zones within the intrusion and the formation of potential associated ore deposits. This study offers a good opportunity to understand the petrogenetic processes leading to the formation of mineralized post-collisional granites throughout the ANS and elsewhere.

2. Field work

The distribution of rare-metal bearing granite intrusions in the Eastern Desert of Egypt is shown in Fig. 1a. The Mueilha area (#9) is located in the southern part of the central Eastern Desert between latitudes 24^{o} $52^{\backslash}03^{\backslash\backslash}$& 24^{o} $53^{\backslash}42^{\backslash\backslash}$N and longitudes $34^{o}00^{\backslash}00^{\backslash\backslash}$& 34^{o} $02^{\backslash}$ $10^{\backslash\backslash}$E, on the southern side of the Idfu-Mersa Alam road. The intrusion appears in satellite imagery as a light-colored area (Fig. 1b). Apart from the Mueilha intrusion itself, the study area is mainly covered by an island-arc assemblage (Fig. 1c) of highly foliated metasedimentary biotite and hornblende schists. The field relationships between the different rock types of the Mueilha intrusion and their country rocks are shown in a schematic cross-section in (Fig. 1d).

The Mueilha intrusion is easily distinguished in the field and forms an ellipsoidal stock covering ~7.5 km^2, elongated in a NE–SW direction. Contacts between the Mueilha intrusion and its metamorphic country rocks are knife-sharp (Fig. 2a, b). There are many dyke swarms that cut the country rocks but are truncated by the boundaries of the Mueilha intrusion. Apophyses of the Mueilha intrusion extend into the adjacent metasediments for several tens of meters (Fig. 2c). Also, small diapirs are observed piercing the country rocks (Fig. 2d). A set of vertical to near-vertical fractures and faults crosscut the Mueilha intrusion and extend into the surrounding metasediments. The Mueilha intrusion consists entirely of fine- to medium-grained, holocrystalline, leucocratic granite. Xenoliths, enclaves, or mafic dikes are absent, except for a few rare metasedimentary blocks along the southern periphery of the intrusion.

In the field the Mueilha intrusion consists of two main rock types: the red and white granites. Contacts between the types are irregular and may be either sharp or gradational, indicating syn-contemporaneous emplacement (Fig. 2e). A few roof pendants of the white granite are observed near the upper border of the red granite (Fig. 2f), which indicates that, even though the two types are syn-contemporaneous, the white granite is older than the red granite. The difference in field-exposure color is also apparent in hand specimens (Fig. 3a-d). The red granites, which constitute the main mass of the intrusion, include alkali feldspar granite and muscovite granite varieties (Fig. 3 a, b). Both are medium-grained, with equigranular to inequigranular textures characteristic of hypabyssal emplacement. A less common pinkish-white garnet-bearing granite (Fig. 3c) is exposed near the contact between the red granite and metasedimentary country rocks; in Fig. 1c and in the following discussion the garnet-bearing variety is grouped with the red granites. The white phase consists of albite granite (Fig. 3d), partly porphyritic in texture. In a few outcrops, the alkali feldspar granite intrudes both muscovite granite and albite granite and contains very small xenoliths (1-5 cm) of albite granite.

Pegmatite dikes and pockets are concentrated near the margins of the intrusion. Contacts between the pegmatite dikes and host granites are typically sharp, whereas pegmatite pockets (from a few to tens of centimeters in diameter) display gradational contacts with the host granite. Rarely, pegmatite dikes extend into the surrounding metamorphic rocks proximal to the intrusion. Pegmatitic dikes display clear zoning from fine grained albite-rich aplitic margins to cores of coarse K-feldspars. There are many nests and veins of fluorite around the outer margins of the intrusion. Also, thin veins of greisen occur along the southern margin. Despite clear evidence of fluid activity within the intrusion and of dikes and apophyses extending beyond the sharp intrusion boundaries into the country rock, there is no field evidence of fluid alteration of the country rocks themselves. In contrast to the well-developed alteration haloes around many other magmatic cupolas in the ANS, fluid infiltration of the metamorphic country rocks around the Mueilha intrusion appears to have been limited, suggesting a regime dominated by brittle fracture and discrete fluid conduits rather than pervasive infiltration. As such, alteration of the country rocks was not a focus of this study.

3. Petrography

The petrographic descriptions of the rocks of the Mueilha intrusion are divided below by rock type.

3.1. Alkali feldspar granite

The alkali feldspar granite is essentially composed of alkali feldspars and quartz with a lesser amount of plagioclase and rare biotite. Fe-Ti oxides, Nb-Ta oxides, muscovite and zircon are accessory minerals. Secondary minerals include epidote, chlorite and sericite. The rock exhibits holocrystalline hypidiomorphic texture. Alkali feldspars occur as anhedral to subhedral crystals of orthoclase and perthite with fewer crystals of microcline. The perthite crystals show various textures, including patchy, vein, flame and zebra types. Orthoclase shows simple twinning, while microcline exhibits cross-hatch tartan twinning. Plagioclase occurs as euhedral to subhedral crystals characterized by albite twinning; many of them are partially altered to sericite and kaolinite. Rare plagioclase inclusions are observed within the perthite crystals (Fig. 4a). Quartz occurs as rounded to subhedral crystals that contain small inclusions of zircon (Fig. 4b) as well as muscovite filling the cracks (Fig. 4b). Some small quartz aggregates are also found filling fractures in crystals and in the interstices between the grains. Biotite is the only mafic phase among the main minerals in the alkali feldspar granite. It occurs as brown to greenish-brown fine subhedral crystals with strong pleochroism, slightly altered to chlorite and opaques. Rarely, biotite occurs as fine inclusions within large K-feldspar and quartz crystals.

Nb-Ta oxides occur as anhedral, subhedral, or euhedral prismatic crystals and show variation in color from black to deep brown. The zoned crystals may exhibit concentric zoning with columbite cores surrounded by a mottled or patchy zones of fluorcalciomicrolite and wodginite (Fig. 4c). The mineral names in Fig. 4c and other backscatter images are based on microprobe and SEM analyses (see section 5. Mineral chemistry).

3.2. Muscovite granite

Muscovite-bearing granite is essentially composed of K-feldspars and quartz, with lesser amounts of plagioclase and muscovite. The accessory minerals include Fe-Ti oxides, Nb-Ta oxides, zircon, apatite and fluorite. K-feldspars occur as subhedral to anhedral crystals showing perthitic texture and appear to be turbid due to staining by fine red iron oxides. K-feldspars enclose plagioclase crystals as well as small muscovite and quartz crystals.

Quartz occurs as anhedral crystals with rare small inclusions of muscovite and plagioclase and scarce fractures filled with muscovite. Plagioclase occurs as euhedral to subhedral small plates characterized by lamellar albite twinning. A few crystals are mildly altered to sericite and muscovite. Both primary and secondary muscovites are recognized in the muscovite granite. The first occurs as subhedral to euhedral crystals with perfect cleavage and high interference colors (Fig. 4d), while the latter occurs mainly as fine anhedral crystals replacing feldspars. Nb-Ta oxides occur as very fine anhedral crystals (Fig. 4e).

3.3. Garnet-bearing granite

Toward the lateral margins of the Mueilha intrusion, the color gradually changes from red to pinkish-white in the garnet-bearing granite. The garnet-bearing granite has holocrystalline texture composed mainly of K-feldspars, quartz and plagioclase with a few garnets. Fluorite, apatite, zircon, Fe-Ti oxides and Nb-Ta oxides are accessory minerals.

K-feldspars (perthite, orthoclase and microcline) occur as subhedral to anhedral crystals that are slightly to moderately altered. Large K-feldspar crystals enclose small inclusions of quartz and plagioclase. Myrmekitic texture appears in this rock type, especially on the margins of K-feldspar crystals (Fig. 4f). Perthite is the dominant K-feldspar and shows a variety of textures including veined, flame and patchy. Orthoclase occurs as large crystals showing simple twinning. Microcline shows its characteristic tartan twinning. Quartz occurs as anhedral large crystals or as small aggregates in the interstices between the other constituents. Wavy extinction is apparent in some samples, suggesting minor deformation. Some discrete crystals of quartz display micrographic intergrowths with K-feldspars. Plagioclase occurs as subhedral to anhedral crystals including albite and oligoclase. Some plagioclase crystals are sericitized and kaolinitized, specially in the cores. Some albite crystals are secondary, replacing K-feldspars and preserving some perthitic and microcline textures. Also, rare albite crystals are enclosed by large crystals of K-feldspars.

Garnet occurs as euhedral to subhedral crystals, crossed by cracks, with chloritized rims (Fig. 4g). A few inclusions of quartz, zircon and opaques are observed in the large garnet crystals. The cracks in some large crystals of garnet are filled with secondary minerals including quartz and muscovite. Fluorite is the most abundant accessory mineral, occurring mainly in interstices between other minerals or as idiomorphic discrete crystals. Locally, veinlets of fluorite are observed cutting the other minerals. These features indicate that the fluorite crystallized at a late stage, after the bulk of the rock-forming minerals. Rare muscovite occurs as anhedral flakes among the other constituents and as fine inclusions in the quartz. Rare small subhedral to anhedral corroded crystals of Nb-Ta oxides are observed in the garnet-bearing granite (Fig. 4h).

3.4. Albite granite

The albite granite is mostly massive and white in color, spotted with small dark crystals of Nb-Ta oxides. It shows fine- to medium-grained, hypidiomorphic and sometimes porphyritic texture. Some samples of the albite granite are sheared; these differ from massive phase due to enrichment of secondary muscovite. The albite granite shows evidence for various degrees of alteration and brittle deformation.

Mineralogically, the massive albite granite consists of quartz and albite with lesser amounts of K-feldspar. The accessory phases include Fe-Ti oxides, biotite, zircon, garnet, Nb-Ta oxides, fluorite and apatite. Albite is the most abundant mineral, occurring as subhedral to euhedral crystals or as small interstitial laths. It also occurs as small euhedral laths included in quartz and K-feldspars. Some albite crystals, especially the cores, are slightly altered. A few earlier albite crystals are rimmed by second-generation albite. Quartz occurs as large anhedral crystals or as fine interstitial aggregates. A few quartz crystals have fine inclusions of albite or muscovite. Rarely, large quartz crystals display snowball texture, formed by concentrically-grown albite laths within quartz (Fig. 4i). K-feldspars — appearing as highly fractured, subhedral to anhedral perthite and microcline crystals — are modally rare in the albite granite. The perthite crystals show flame type and simple twinning. Microcline shows tartan twinning and is partly replaced by secondary albite with preservation of original crystal habit. Myrmekitic texture occurs on the boundaries of many K-feldspar crystals. Some K-feldspars are partially replaced by albite and/or muscovite.

The albite granite sporadically contains subhedral to euhedral, optically homogeneous garnets with variable grain size (0.1-0.5 mm). The garnet shows no reaction rims or evidence of intergrowth with any adjacent minerals. Some garnet crystals are highly fractured. Muscovite is colorless to pale green and forms fine anhedral flakes within K-feldspars (Fig. 4j) or replacing biotite. Fluorite occurs as small anhedral crystals interstitial to the feldspars or, rarely, as veins along through-going fractures that suggest a deuteric origin (Tollo et al., 2004). Columbite is the most common Ta-Nb oxide and occurs in various forms associated with biotite (Fig. 4k) or interstitial to feldspar crystals. It occurs commonly as prismatic and tabular crystals with well developed crystal faces and exhibits color variation suggestive of zoning (Fig. 4l). More Ta-rich grains occur as very small disseminated anhedral specks or as thin rims around columbite; these are too small to analyze and so cannot be confidently identified as either Ta-bearing columbite or as tantalite.

3.5. Pegmatites

The pegmatite veins that cut the Mueilha granites show variable colors, grain sizes, textures and mineral compositions. Based on their mineral composition, vein cores are K-feldspar-rich pegmatite and vein margins are albite-rich pegmatite. The K-feldspar-rich pegmatite, pink in color and medium- to very coarse-grained, consists mainly of K-feldspars with lesser amounts of quartz, albite and muscovite. The accessory minerals include Fe-Ti oxides, biotite, zircon, fluorite and apatite. K-feldspars occur as very coarse subhedral and anhedral crystals that include perthite, microcline-perthite and orthoclase. Some large crystals of K-feldspars enclose small crystals of albite, iron oxides and zircon. Quartz shows undulose extinction and a few crystals have very fine inclusions of K-feldspars and albite.

The albite-rich pegmatite consists of albite, quartz, K-feldspar, biotite and muscovite. The accessory minerals include opaques, fluorite, and zircon. Albite is the most common mineral and occurs as euhedral to anhedral prismatic crystals characterized by lamellar twinning. Some albite crystals show bent and broken twin planes due to later deformation. Other albite crystals are highly altered to sericite and muscovite, especially in their cores. K-feldspar crystals show perthitic texture and microcline cross-hatching, and rarely include small inclusions of quartz and muscovite. A few quartz crystals are graphically intergrown with albite or contain small inclusions of rounded to euhedral albite. Muscovite is found as small flakes among the other constituents or enclosed in K-feldspar.

3.6. Quartz veins

Quartz veins consist of quartz with minor amounts of fluorite and chlorite. The quartz crystals are medium- to coarse-grained and subhedral. Along contacts with the country rocks, quartz occurs as sub-parallel needle-shaped aggregates of fine grains. Quartz veins contain many inclusions of the mineral assemblage of the country rocks such as pyrite and feldspars. Many quartz crystals show wavy extinction and fractures that indicate a history of deformation.

4. Analytical techniques

Optical mineral identifications were refined where necessary with back-scattered electron imaging, energy-dispersive X-ray analysis, and X-ray mapping on a scanning electron microscope. The microprobe analyses were carried out the CAMECA SX100 electron probe at the Department of Geosciences, University of Oslo. The run conditions were 15 kV accelerating voltage, 15 nA beam current, 2 μm beam diameter and 10 seconds count time on peak and 5 seconds for both low and high backgrounds. A ZAF matrix correction routine was used. Calculations of the mineral structural formulae used appropriate software including custom spreadsheets and Minpet (Richard, 1995).

Fifteen rock samples of the Mueilha intrusion were selected, based on the petrographic studies, for major, trace and rare earth element analysis at Activation Laboratories Ltd. (Actlabs, Canada). The bulk chemistry of the representative samples was determined by a combination of ICP-AES and ICP-MS. The major oxides were measured by lithium metaborate/tetraborate fusion ICP-AES (package code 4B). Trace and rare earth elements were measured using ICP-MS (package code 4B2) following lithium borate fusion and acid digestion. The detection limits for the major oxides are between 0.01 wt. % and 0.04 wt. %, for trace elements between 0.1 and 0.5 ppm, and for the rare earth elements between 0.01 and 0.05 ppm. Loss on ignition (LOI) was determined by weight difference after firing in air at 1000 ºC. Precision and accuracy were monitored by analysis of international reference materials and replicate analyses and are 1% for major elements and 2 to 5% for trace elements.

5. Mineral chemistry

Feldspars, micas, Nb-Ta oxides, garnet, and zircon were analyzed by electron microprobe, allowing assignment of systematic mineral names and offering constraints on the origin and evolution of the granites under investigation. All electron microprobe data are given in the supplementary tables (1S-10S).

5.1. Feldspars

Feldspars were analyzed in all the rock types of the Mueilha intrusion. The chemical analyses and structural formulae (on the basis of 8 oxygen atoms) of the analyzed feldspars are given in supplementary tables 1S, 2S and 3S. The analyzed feldspars include K-feldspars, albite and plagioclase. K-feldspars and albite were found in all rock varieties; plagioclase only in the alkali feldspar granite and muscovite granite.

All the analyzed K-feldspar crystals are homogenous near end-member $KAlSi_3O_8$, with low Na_2O (<0.43 wt. %) and CaO contents (<0.1 wt. %). The analyzed albites are near end-member $NaAlSi_3O_8$ with low K_2O (<0.89 wt. %) and CaO (<0.1 wt. %.) contents. No attempt is made here to reconstruct original compositions of perthite crystals or other exsolved features. The analyzed plagioclase is exclusively oligoclase (An_{12-17}).

5.2. Micas

Both muscovite and biotite were analyzed. Muscovite was found in all rock types, whereas biotite only in alkali feldspar granite and muscovite granite. The chemical analyses of muscovite and their structural formulae (on the basis of 22 oxygen atoms) are given in supplementary table 4S. Primary muscovite is considerably higher in TiO_2, Al_2O_3 and Na_2O, but lower in MgO, than secondary muscovite. The primary muscovite has TiO_2 > 0.33 wt. %, comparable to muscovite of magmatic origin (e.g. Zen, 1988). The analyzed muscovites plot in the primary and secondary muscovite fields (Fig. 5a), on the discrimination diagram of Miller et al. (1981), concordant with expectations from texture.

The chemical analyses of biotite and their structural formulae (on the basis of 22 oxygen atoms) are given in supplementary table 5S. The analyzed biotite has Al_2O_3 contents between 21.0 and 24.1 wt.% with an average of 22.1 wt.%, FeO between 13.6 and 19.2 wt.% with an average of 17.1 wt.%, MgO between 2.0 and 3.4 wt.% with an average of 2.5 wt.%, and K_2O between 9.1 and 10.0 wt.% with an average of 9.8 wt.%. On the discrimination diagram of Nachit et al. (2005), all specimens are classified as annite. The analyzed biotite crystals have chemical characteristics of primary igneous biotite (Fig. 5b).

Using the biotite discrimination diagram of Abdel-Rahman (1994), the analyzed biotite plots in the peraluminous field (Fig. 5c). Nachit et al. (1985) used the chemical composition of biotite to discriminate among peraluminous (P), calc-alkaline (C), subalkaline (SA) and alkaline-peralkaline (A-PA) granites. On the Mg vs. Al plot, the analyzed biotite crystals plot in the peraluminous field (Fig. 5d).

5.3. Nb-Ta oxides

The analyzed Nb-Ta oxides include columbite, fluorcalciomicrolite and wodginite. Columbite is the main primary Nb-Ta bearing phase in the Mueilha granite. None of the analyzed spots are tantalite, though some high-backscatter spots too small for quantitative analysis are observed. Fluorcalciomicrolite and wodginite are secondary phases. The chemical analyses of Nb-Ta oxides and their structural formulae are given in supplementary tables (6S, 7S, 8S).

Nb_2O_5 (42.3-70.9 wt. %) and Ta_2O_5 (8.9-39.6 wt. %) are the major oxides in columbite (supplementary table 6S) with subordinate MnO (6.0-10.4 wt. %) and FeO

(6.8-10.4 wt. %). The concentrations of other oxides such as SiO_2 (0.6-4.9 wt. %), TiO_2 (<0.2 wt. %), and SO_3 (<0.11 wt. %) are low. Analytical points with significant SiO_2 are considered to be altered. Columbite has Ta/(Nb+Ta) ratios between 0.07 and 0.36 and Mn/(Mn+Fe) ratios between 0.43 and 0.58; hence various points are classified as either columbite-(Mn) or columbite-(Fe). Compositions within and among grain cores form a coherent trend when plotted on a Mn/(Fe+Mn) vs. Ta/(Nb+Ta) diagram (Fig. 5e), whereas high-backscatter points near rims (Fig. 4c, k) define a separate population enriched in Ta/(Nb+Ta) at constant Mn/(Mn+Fe).

Fluorcalciomicrolite is observed only in the garnet-bearing granite and alkali feldspar granite. It forms well-defined overgrowth or replacement mantles around primary columbite, separated by sharp boundaries. The major oxides of the fluorcalciomicrolite are Ta_2O_5 (40.8-47.3 wt.%), Nb_2O_5 (24.2-27.9 wt.%) and CaO (11.0-13.0 wt.%) with lesser amounts of Na_2O (2.8-4.0 wt.%) and SiO_2 (5.2-6.4 wt.%). Again, significant Si is considered evidence of late alteration. The concentrations of other oxides such as TiO_2 (0.4-0.5 wt.%), FeO (<0.03 wt.%) and SO_3 (<0.04 wt.%) are low (supplementary table 7S). Fluorine was not quantitatively analyzed on the electron microprobe, but it is evident in energy-dispersive X-ray spectra and X-ray maps taken by scanning electron microscope, with semi-quantitative concentration estimates sufficient to confidently assign the name fluorcalciomicrolite to this material.

Wodginite is commonly encountered in the garnet-bearing granite and alkali feldspar granite as part of the alteration mantle around grains of columbite and fluorcalciomicrolite (Fig. 4c). Nb_2O_5, Ta_2O_5 and MnO are the major oxides, while concentrations of other oxides (SiO_2, TiO_2 and SO_3) are low (supplementary table 8S).

5.4. Garnet

Garnet compositions were determined in the albite granite and garnet-bearing granite. The chemical analyses, structural formulae, and end-member fractions of garnet (on the basis of 12 oxygen atoms) are listed in supplementary table 9S. All the analyzed garnets are spessartine-rich solid-solutions with subordinate amounts of almandine. Spessartine and almandine together constitute more than 96% for all analyzed garnet crystals; amounts of other garnet components are all very low. The end-member mole fraction range is: spessartine (65.31-72.30 mol. %), almandine (26.29-33.3 mol. %), pyrope (0.71-2.83 mol. %), grossular (< 1.0 mol. %) and andradite (<0.02 mol. %). The chemical homogeneity and subhedral to euhedral form suggest that the analyzed garnets are magmatic in origin. On a Mn-Mg-Fe ternary diagram of Miller and Stoddard (1981), the chemical analyses of the analyzed garnet plot in the field of magmatic garnet (Fig. 5f). The garnet compositions in the Mueilha granite (i.e., low MgO and high MnO) are similar to those commonly crystallized from silicic magma at low pressure (Patiño Douce 1999; Abuamarah et al., 2019; Azer et al., 2019).

5.5. Zircon

Selected zircon compositions were determined in muscovite granite and alkali feldspar granite. Chemical compositions and calculated structural formulas of zircon crystals from both varieties are given in supplementary table 10S. The analyzed zircons have somewhat low totals (96.62-98.38 wt. %). Energy-dispersive X-ray analysis shows that no elements present at levels above a few tenths of a weight percent were left out of the electron probe protocol. Hence the low totals likely reflect either metamict zircons or poor polish. The analyzed zircon crystals show very limited variations in their chemical compositions with 31.0 to 31.3 wt.% SiO_2, 63.0 to 64.4 wt.% ZrO_2, and 1.8 to 2.0 wt.% HfO_2. Other oxides occur at or below detection limits.

6. Whole rock geochemistry

6.1. Geochemical characteristics

The concentrations of major oxides, some trace elements, and REE were analyzed in 15 samples of Mueilha granite. The whole-rock chemical analyses, CIPW norms, and REE concentrations are given in Tables 1, 2 and 3 respectively. The granites are all highly evolved, with silica contents 71.9-78.4 wt. %. The lowest silica contents were found in the garnet-bearing granite (≤73.3 wt. % SiO_2) and albite granite (73.1-74.4 wt. % SiO_2). Total alkalis (Na_2O+K_2O = 8.4-11.3 wt. %) and differentiation index (D.I. = 91-98) are high. K_2O/Na_2O decreases and Al_2O_3 increases as SiO_2 decreases from red to white granites, reflecting the exchange of modal K-feldspars for albite. Most of the analyzed samples have normative corundum (0.2-2.0 wt. %), while a few samples have normative acmite (0.2-0.9 wt. %) and Na-metasilicate (0.6-1.5 wt. %). The presence of normative acmite and Na-metasilicate in a few samples can be attributed to the high contents of total alkalis (10.42-11.28 wt. %) in these samples.

Classification of the studied granites using whole-rock geochemistry supports our field and petrographic studies. On the R1-R2 discrimination diagram of De la Roche et al. (1980), the Mueilha granites plot in the alkali granite field, except for one sample of garnet-bearing granite (MH14) that plots in the quartz-syenite field (Fig. 6a). This classification is supported by the normative $Q^{/}(F^{/})$-ANOR (Fig. 6b) classification diagram of Streckeisen and le Maitre (1979), on which the analyzed samples fall mainly in the alkali feldspar granite field, except one albite granite sample and one garnet-bearing granite sample that straddle the boundary of the alkali feldspar granite and quartz syenite fields.

Selected major oxides of the Mueilha granites are plotted against in SiO_2 variation diagrams in Fig. 7. The entire suite defines continuous trends in all oxides without any compositional gaps. TiO_2, Al_2O_3, CaO, Na_2O contents increase while SiO_2 and K_2O decrease in the sequence alkali feldspar granite, muscovite granite, albite granite, garnet-bearing granite. Fe_2O_3 shows no trend among the red granite varieties, but is offset to lower values in the albite granite. The other major oxides are all at low concentrations and are weakly correlated with SiO_2 and with one another.

Trace element contents of the measured samples vary over roughly a factor of two within the entire Mueilha suite for most elements, but the rare earth elements and Y vary by an order of magnitude. The concentrations are well-correlated with SiO_2 for most elements. Similar variability has been described in other rare-metal bearing granites in the Eastern Desert of Egypt (Abuamarah et al., 2019; Azer et al., 2019; Heikal et al., 2019). Selected trace elements are plotted against SiO_2 in Fig. 8. Rb, Nb, Y, Th, U and Zn decrease systematically from red to white granites (Fig. 8a), whereas Sr, Ba, V, Ga, Ni, Cu, Sc and Cr all increase with decreasing SiO_2 content (Fig. 8b).

6.2. Spider diagrams and REE characteristics

Mid-ocean ridge basalt (MORB) normalized multi-element trace element patterns of the Mueilha granites, using normalization values of Pearce (1983), are shown in Fig. 9a. The studied granites show overall similarity in the trace element patterns for all the samples, with enrichments of certain elements up to three orders of magnitude relative to MORB. They are characterized by clear depletions in Sr, Ba, P and Ti, reflecting a much larger role for either residual or fractionated feldspars, apatite and Fe-Ti oxides compared to MORB petrogenesis (Wu et al., 2002). The difference in Y concentrations between, on the one hand, garnet-bearing and albite granites and, on the other hand, alkali feldspar and muscovite granites is large enough to be seen even at the scale of Fig. 9a.

REE concentrations of the Mueilha granites are given in Table 3. They show subparallel chondrite-normalized patterns (Fig. 9b; normalization of Evensen et al., 1978); enrichment of HREE relative to LREE is reflected in $(La/Lu)_n$ values from 0.09 to 0.31. The albite granite and garnet-bearing granite samples have relatively lower REE abundances (especially the moderately heavy REE from Gd to Er) than the red granite samples. The lower abundance of REE-bearing accessory minerals noted petrographically in the white granite correlates with the smaller whole-rock REE concentrations seen in Fig. 9b. The REE patterns show strongly negative Eu anomalies, with (Eu/Eu*) = 0.01-0.08. Together with the large negative anomalies in Ba and Sr, this also suggests sequestration of feldspar, either during formation of the crustal source, during melting of that source, or during differentiation of the magma.

6.3. Magma type and tectonic setting

The Mueilha granites are highly fractionated with slightly peraluminous to slightly peralkaline character. The discrimination diagram of Sylvester (1989), intended for discriminating among rocks with $SiO_2 > 68$ wt.%, places the Mueilha granites in the highly fractionated calc-alkaline field (Fig. 10a). The alkali feldspar granite and muscovite granite have peraluminous character (Fig. 10b), with alumina saturation index [ASI = molar ratio $Al_2O_3/(CaO+Na_2O+K_2O)$] greater than unity (Table 1). This is consistent with their normative corundum contents (0.24-2.01 wt. %, Table 2), the presence of primary muscovite in most samples, and the mineral composition of biotite as noted above (Fig. 5c, d). Only the garnet-bearing and albite granites extend below ASI = 1 into the metaluminous and peralkaline fields. Most samples have agpaitic index values [AI = molar (Na+K)/Al] greater than 0.87 (0.85-1.09, av. 0.94; Table 1), indicating some degree of alkaline character (Liégeois et al., 1998).

The Mueilha granites have many characteristics similar to A-type granites, such as high Ga/Al, Nb, Zr, Y, Ta and Th and significant depletion in MgO, CaO and P_2O_5 (e.g. Bonin, 2007; Eby, 1992; Whalen et al., 1987). On the Ga/Al vs. FeO/MgO discrimination diagrams of Whalen et al. (1987), the Mueilha granites display clear A-type character (Figs. 11c). Extensive fractional crystallization of I-type calc-alkaline granites can produce A-type residual liquids (e.g., Clemens et al., 1986; Whalen et al., 1987). In the present case, the discrimination diagram of Frost et al. (2001) indicates a typical A-type signature (Fig. 10d). On the FeO-10*MgO-MnO ternary discrimination diagram of Zhang et al. (2012) for garnet, the analyzed garnets plot close to the boundary of the A-type granite field (Fig. 10e), with some unusual additional Mn enrichment. On the Y/Nb vs. Rb/Nb diagram of Eby (1992), the alkali feldspar and muscovite granite samples plot in the A2-type granite field (Fig. 10f), while the garnet-bearing and albite granites are shifted from this field due to their depletion in Y.

Using the Y vs. Nb and Rb vs. Y+Nb tectonic discrimination diagrams of Pearce et al. (1984), the Mueilha granite samples plot clearly in the within-plate granite field (Fig. 11a). On the multicationic diagram of Batchelor and Bowden (1985), the red granites plot in the post-orogenic granite field (Fig. 11b) while the white granites extend towards the anorogenic field. On the Rb-Hf-Ta ternary diagram of Harris et al. (1986), the samples form a trend from the late- to post-collision field into the within-plate field (Fig. 11c). In summary, numerous discriminants, based on whole-rock and mineral major and trace element chemistry, consistently indicate a within-plate, peraluminous, post-collisional, A-type character for the red granites. The white granites are anomalous in some ways, perhaps due to post-magmatic alteration of their bulk chemistry.

7. Petrogenesis

7.1. Source rocks

The Mueilha intrusion consists of highly fractionated A-type granites. A number of potential sources and models of formation have been proposed for the A-type rocks of the Eastern Desert of Egypt (e.g. Sami et al. 2017, 2018; Heikal et al, 2019; Abuamarah et al., 2019, Azer et al., 2019). The large differences in major and trace element concentrations and isotope ratios among various A-type granitic rocks in the Eastern Desert of Egypt strongly suggest that a variety of processes and sources were involved in their genesis (Farahat et al., 2007; Ali et al., 2012). In the particular case of the Mueilha intrusion, it been assigned to either magmatic (e.g. Salem et al., 1985; Morsy and

Mohamed, 1992; Abou El Maaty and Ali Bik, 2000) or metasomatic origins (e.g. El-Galy et al., 2016; Abu El-Rus et al., 2017). In fact, the distinction between magmatic and metasomatic processes may not be as absolute as once thought (Lundstrom, 2016; Azer et al., 2019), and transitional models may provide a path to reconciling the available evidence.

Salem et al. (1985) concluded that the primary magmatic phase of the Mueilha intrusion was a late- to post-orogenic muscovite granite derived from crustal sources that evolved by fractional crystallization and some part of the intrusion was albitized by sodium metasomatism (see also Hassanen et al., 1995). Morsy and Mohamed (1992) argued that fluorine was an important complexing anion in the Mueilha magma and that this helps to explain their fractional crystallization pathway. Abu El-Rus et al. (2017) proposed that all the exposed Mueilha granites developed through metasomatic reactions involving hydrothermal fluids in the already-consolidated medium grained cupola of a tonalitic/granodioritic magma chamber. Curiously, they suggested that the albite granite (in their terminology, the milky white granite) was the least-altered exposed material, which changed gradationally into more altered red granites as a result of metasomatic enrichment in potassium. The field, petrographic, and geochemical evidence summarized below in section 7.3 rejects the model proposed by Abu El-Rus et al. (2017), showing that the red granite preserves numerous magmatic signatures that are overprinted in the white granite.

The treatment of the entire Mueilha intrusion and all its subtypes of granite as cogenetic is consistent with the gradational petrologic boundaries within the intrusion, the similarity of the normalized trace element and REE patterns of all analyzed samples (Fig.

9) and the coherent trends without any clear compositional gaps in major and trace elements variation diagrams for both compatible and incompatible elements.

The absence of intermediate or mafic igneous rocks in the Mueilha intrusion, even as enclaves or xenocrysts, argues against derivation by extensive fractionation crystallization of a mantle-derived mafic magma. Indeed, generation of highly evolved A-type granites by continuous fractional crystallization from parent mafic magma is inefficient and would require at least nine times the volume of the final product in initial mafic magma (Turner et al., 1992). Rather, the geochemistry, especially of the red granites, points to a felsic primary magma generated by partial melting of a juvenile crustal source. On the Y/Nb vs. Rb/Nb plot (Fig. 10f), the Mueilha red granites plot in the A2-type granite field, which Eby (1992) attributed to magmatic sources in continental crust or underplated mafic material after a cycle of continent-continent collision or island-arc magmatism. Although Nb and Ta are geochemically similar in many ways, crustal sources have elevated Nb/Ta compared to mantle sources (Smirnov et al., 1983), consistent with the higher contents of Nb (31-74 ppm) than of Ta (15-25 ppm) in the Mueilha granites and the dominance of columbite over tantalite. Among potential crustal sources for the parental melt of the Mueilha granites, the Neoproterozoic upper crustal basement rocks include schists and gneisses, metagabbro-diorite and I-type calc-alkaline granitoids. The Mueilha red granites are mildly peraluminous in character. Experimental results show that melting of schists and gneisses, whether their protoliths were pelitic sediments or quartz-rich aluminous greywackes, yields peraluminous compositions (Montel and Vielzeuf, 1997), leading us to favor the metasedimentary schists and gneisses of the basement complex as a likely source for the primary magma of the Mueilha granites.

Melting of the crustal rocks requires an elevated geotherm, which can occur along large-scale intra-continental fault systems and shear zones (Black et al., 1985) without development of mature rifts. The importance of such a mechanism in the post-collisional phase of the ANS is supported by the distribution of post-collisional A-type rocks, including rare-metal granites in the Eastern Desert of Egypt; they are associated with major faults, shear zones, and deep-seated fractures (e.g., Morsy and Mohamed, 1992; Mohamed, 1993). At deeper levels, anomalously elevated temperatures that result in partial melting of relatively thin continental crust are often assigned to ascent and underplating of mantle-derived mafic magma that, in turn, were generated by post-orogenic lithospheric delamination. The lithospheric delamination model is commonly invoked to explain magmatism in the post-collisional stage (950-610 Ma) of the ANS (e.g. Avigad and Gvirtzman, 2009; Be'eri-Shlevin et al. 2011). The dyke swarms that cut the country rocks of the Mueilha intrusion support an extensional tectonic regime during its emplacement. Also, the common occurrence of core complexes, strike–slip faults, shear zones, and dike swarms in the basement rocks of Egypt (Blasband et al., 2000; Avigad and Gvirtzman, 2009) support the presence of an extensional regime during the post-collisional stage in the north ANS. Faults and shear zones help transmit anomalous heat flow to the middle crust more rapidly than simple conduction allows, enhancing partial melting of supracrustal sequences and formation of peraluminous A-type granites.

The proposed model for the tectonomagmatic evolution of the Mueilha intrusion through partial melting of the juvenile crust of the ANS during the post-collisional phase is shown in Figure 13. In this model, crustal and lithospheric thickening during the collisional phase of assembly of the ANS is followed by slab break-off and lithospheric delamination. The delamination forces upwelling and partial melting of hot asthenosphere, resulting in uplift and extensional doming of overlying crust. The mantle-derived mafic magma underplate the crust, providing a source for elevated heat flow and evolved magma products that ascend into the lower crust and, along shear zones, ultimately into the upper crust. Partial melting results in formation and emplacement of coeval post-collisional calc-alkaline (from mafic underplate or crustal components) and alkaline (from metasedimentary components) magmas. In the ANS, the earlier stages of post-collisional alkaline magmatism overlap with the timing of the later stages of calc-alkaline magmatism (Be'eri-Shlevin et al., 2011; Eyal et al., 2010). Storage and hybridization of the primary magma then promotes evolution to highly fractionated A-type granites. The abundance of strike-slip faults and shear zones during the post-collisional stage helps provides conduits for passage of these magmas to the shallow crust, explaining their common alignment along such structural trends.

7.2. Geodynamic emplacement of Mueilha granites

The Mueilha intrusion probably represents a magmatic cupola above highly fractionated A-type magma. The present study indicates that the southern portion of the Mueilha intrusion (albite granite) represents the preserved remnants of the apex of the magma, exposing a shallower level of emplacement, while the main portion of the Mueilha intrusion represents a deeper level. The intrusion of Mueilha granite appears to have reached subvolcanic levels based on the porphyritic texture of the white albite granite along the upper contact. Subsequently, the granite magma crystallized, presumably from all its margins (although the lower contact is not exposed), forming the different types of red granite. The residual melt became enriched in water, alkalis, and fluorine, which led to escape of segregated fluids upwards, causing hydrofracturing of the overlying granite. The fluids caused greisenization and created pegmatites and quartz–fluorite veins that cut the outer parts of the Mueilha intrusion and its surrounding country rocks (e.g., Schmitz and Burt, 1990). Alkalis liberated from feldspars destroyed during the greisenization caused local albitization in the outer and uppermost part of the magma chamber, generating the transitional pink garnet-bearing granite and the fully albitized white granite. Also, porphyritic snowball quartz crystals were produced in the apical and outer parts of the chamber, possibly a signature of "compositional quenching" whereby the solidus was shifted upwards in temperature as volatile activity rapidly declined (volatiles may have been either lost or incorporated into solid phases). The fine-grained varieties of albite granite with porphyritic texture might be a result of pressure quenching related to opening of fractures and vigorous escape of volatiles, perhaps associated with volcanic activity above the magma chamber.

The mode of emplacement of the Mueilha intrusion is very similar to the Abu Dabbab and Nuweibi intrusions in the Eastern Desert of Egypt (Azer et al., 2019; Abuamarah et al., 2019). Each of these intrusions is divided into hypabyssal and porphyritic varieties suggesting that a gradient in emplacement depth extending to very shallow crustal levels is preserved and exposed in each case. The boundaries between the magmatic phases in all three of these intrusions are gradational and the near-simultaneous formation of the phases can be established with confidence. Notably, the marginal zones around the Mueilha, Abu Dabbab and Nuweibi intrusions are quite similar, featuring pegmatite stocks, quartz and fluorite veins and greisen.

7.3. Evidence for magmatic vs. metasomatic effects

Rare-metal bearing granites in the Eastern Desert of Egypt have been attributed to various magmatic processes (Morsy and Mohamed, 1992; Mohamed, 1993; Jahn, 1996; Helba et al., 1997; Abou El Maaty and Ali Bik, 2000), to post-magmatic high-temperature metasomatism (El-Galy et al., 2016; Abu El-Rus et al., 2017), or to a combination of magmatic and post-magmatic processes (Abuamarah et al., 2019; Azer et al., 2019; Heikal et al., 2019).

Numerous observations support the magmatic origin of the Mueilha intrusion and document important magmatic signatures that were preserved despite the action of later metasomatic processes. These observations include: (1) the sharp intrusive contacts of the Mueilha granites with the country rocks; (2) coexistence of euhedral to subhedral crystals of primary feldspars, muscovite and biotite; (3) “snowball" quartz, which is generally considered to be a magmatic texture (Vance, 1969; Müller and Seltmann, 1999) in the Mueilha granites, although similar textures have also been interpreted as metasomatic (Beus, 1982; Müller and Seltmann, 1999); (4) enrichment of the entire intrusion in fluid-immobile rare metals, especially Nb and Ta; and (5) gradual increase in REE concentrations from the early phase (albite granite) to late phase (alkali feldspar granite) due to magmatic fractional crystallization.

Although this evidence leads us to conclude that the Mueilha granites are primarily magmatic, effects of hydrothermal fluids and extensive replacement by secondary minerals are observed in a marginal zone occupying the originally apical part of the intrusion. The effects of hydrothermal fluids are mainly manifested in the albite granite and to a lesser extent in the garnet-bearing granite by (1) development of greisen, pegmatites, quartz veins, and fluorite veins along fracture systems; (2) partial replacement of microcline crystals by secondary albite with preservation of the original crystal habit of microcline; (3) overgrowth of secondary albite around primary feldspars and quartz; (4) partial alteration of albite crystals to sericite and muscovite; and (5) presence of biotite relics within secondary muscovite. Abu El-Rus et al. (2017) concluded that the albite granite (milky white granite) of the Mueilha intrusion was unaltered magmatic material that changed gradationally into altered red granites as a result of metasomatic enrichment in K-Si fluids. We concur with Abu El-Rus et al. (2017) that the intrusion is partly magmatic and partly metasomatic product, however, we disagree strongly as to which zone of the intrusion is the primary product and which is the altered product. We present clear textural, mineralogical, and geochemical evidence that the alkali feldspar and muscovite granites are rather fresh magmatic products, while the overlying white granite is highly metasomatized. As metasomatic fluids are buoyant and mostly escape upwards, the placement of the altered phase at the top of the intrusion is physically more plausible.

The presence of pegmatite indicates that the granite melts were vapor saturated during their final evolutionary stage (London, 2015). Volatile concentrations are therefore the key to constraining the fractionation behavior of the Mueilha granites. Pegmatite pockets display gradational contacts with the host granite, indicating that they represent products of *in situ* fractionation of granitic magma.

The occurrence of F-bearing minerals such as fluorite and the alteration of primary Nb-Ta oxides to fluorcalciomicrolite indicate the presence of fluids containing appreciable fluorine (F). The Qz–Ab–Or plots of normative compositions (Fig. 13a) show that the Mueilha granites lie close to the minimum melt composition at 1 kbar with excess H_2O fluid containing 1% to 4% F (Manning, 1981). Increasing water pressure shifts the location of the granite minimum towards the albite vertex, supporting a larger role for fluids in forming the albite granite than the alkali feldspar granite. The source of F-rich fluids in granitic systems has been attributed variously to magmatic (e.g., Cuney et al., 1992) and metasomatic sources (e.g., Nurmi and Haapala, 1986). Although sub-solidus re-equilibration texture and formation of secondary minerals at the expense of K-feldspar and mica occur in the upper zone of the Mueilha intrusion, a magmatic origin for the hydrothermal solutions that affected these granites is favored by the following observations. The transition from red granite to altered white granite is gradational and is associated with pegmatites with gradational boundaries, suggesting that crystallization of the red granites was the source of fluids that ascended and altered the white granites. The crystallization of the Mueilha granite eventually produced a saturated, late-magmatic, F-bearing fluid. The fluids migrated toward the apex of the magmatic cupola, where they reacted with still hot but subsolidus albite granite. It seems unlikely that externally sourced fluids would generate the relations observed.

The chemical composition and texture of garnet can be used to indicate the pressure-temperature-fluid activity conditions of garnet growth and hence at least one stage in the petrogenesis of its host rock (e.g. Whitworth, 1992; Zhang et al., 2012). The very spessartine-rich, subhedral to euhedral garnets in the garnet-bearing phase of the

Mueilha intrusion are consistent with growth from highly evolved, silica-rich magma (Whitworth, 1992). Although the Mn–Mg–Fe ternary composition of the garnets falls within the very broad and permissive magmatic field on the plot of Miller and Stoddard (1981) (Fig. 5f), their high Mn contents place them outside the S-type magmatic field of Dahlquist et al. (2007) and outside any of the granite-type garnet fields in the compilation of Zhang et al. (2012). Yet the compositions of the garnets from the present study are similar to garnet compositions reported from several post-collisional granites in the Eastern Desert of Egypt (Azer et al., 2019; Abuamarah et al., 2019). The most likely resolution of the observation that the garnet compositions in the Mueilha garnet-bearing phase are broadly magmatic and yet anomalous compared to all the standard tectonically-interpreted granite types is that they represent a transitional stage, somewhere on the spectrum from late-magmatic to hydrothermal, having grown from a very H_2O- and F-rich silica-rich peralkaline magma at a temperature below the F-free granite minimum. This is consistent with exposure of garnet-bearing granite as a pinkish-white marginal unit, exposed near contacts between red granite and metasediments.

7.4. Formation of Mueilha granites via crystal fractionation

Field studies, textural and compositional variations of the pluton are consistent with evolution through magmatic fractionation without significant assimilation, leading eventually to fluid saturation and hydrothermal alteration of the upper parts of the pluton. Chemically, assimilation might be difficult to recognize since the country rocks are similar to the likely source rocks, but the near-total absence of stoped blocks, xenoliths, or enclaves supports a negligible role for upper-level assimilation. The geochemical characteristics of the Mueilha granites indicate their evolution as a single magmatic suite from a common parental magma by extensive fractional crystallization. The good correlations between SiO_2 and most major and trace element concentrations (Figs. 8, 9) and the single trend in Rb/Sr vs. Sr (Fig. 13b) are consistent with a cogenetic magmatic suite. The consistent shape of the REE patterns with generally increasing concentrations from the early phase (albite granite) to the late phase (alkali feldspar granite) are likewise consistent with progressive fractional crystallization through the rock types; this is a signature that is relatively insensitive to late alteration. In addition to the albite granite being the earliest phase, a concentric progression of the main red granite phase is apparent, from the marginal garnet-bearing granite inwards to the more evolved muscovite granite and finally the most evolved alkali feldspar granite. The negative P and Ti anomalies of the whole suite indicate that there was a major role for early fractionation of apatite and Fe-Ti oxides. Very pronounced negative Eu anomalies and strong depletion in Ba and Sr imply extensive fractionation of feldspar, beginning at a stage more primitive than any exposed rocks and continuing through the observable outcrop suite.

Zr/Hf and Nb/Ta ratios are generally invariant during common magmatic processes, but undergo significant variation during extreme magmatic fractionation, especially during interactions between magma and water (Ballouard et al., 2016). The Mueilha granites show wide variations in their Zr/Hf (5.9-10.9) and Nb/Ta (1.3-4.4) ratios, indicating extreme magmatic fractionation and fluid interaction. Several rare-metal bearing minerals are present in the Mueilha granites, including columbite, fluorcalciomicrolite and wodginite. These minerals are indicators of high degrees of crystal fractionation (Wang et al., 2017).

7.5. Origin of Nb-Ta oxides

Niobium and tantalum are strategic metals in limited global supply and are generally derived from a small set of important ore minerals. Tantalum and niobium oxides concentrate in a few families of related mineral species including the columbite-tantalite [$(Mn,Fe)Nb_2O_6$] to $(Mn,Fe)Ta_2O_6$] series, the microlite-pyrochlore [[$(Na,Ca)_2Ta_2O_6(O,OH,F)$] to $(Na,Ca)_2Nb_2O_6(O,OH,F)$] series, and the wodginite [$Mn(Sn,Ta, Ti)Ta_2O_8$] group. All of these are known from post-collisional granites in the Eastern Desert of Egypt (e.g. Helba et al., 1997; Abdalmarah et al., 2019; Heikal et al., 2019; Azer et al., 2019). Columbite-(Mn), columbite-(Fe), fluorcalciomicrolite and wodginite are found in the Mueilha intrusion. The identification of Ta-Nb mineralization in the Mueilha granites suggests significant potential of the pluton as an exploration site for rare-metals.

The positive correlations of whole-rock Nb and Ta with increasing SiO_2 in the Mueilha suite indicate that the enrichment of Ta and Nb is largely controlled by magmatic processes; they were not significantly transported or concentrated by the metasomatic fluids that affected the albite granite, although their mineralogical hosts may have been modified locally. Rather, the accumulation of volatiles and low-degree melting components towards the later magmatic stages of the intrusion likely played a role in the enrichment of the red granite phase in rare metals. The solubility of rare metal complexes in magmas decreases with decreasing temperature (Chevychelov et al., 2005), an effect that probably drove crystallization of rare metal minerals in the later phases of the intrusion, especially in the alkali feldspar granite. The inner part of the Mueilha pluton, where the most highly fractionated alkali feldspar granite is exposed, contains notably higher modal abundance of Nb-Ta oxide phases and higher whole-rock Nb-Ta grades than the periphery of the intrusion.

Petrographic examination shows that the Nb-Ta oxides are mainly associated with muscovite and biotite. The magmatic nature of the biotite and muscovite is indicated by their euhedral to subhedral crystal habit (Fig. 4d, k), their presence as inclusions in feldspars and quartz, and their chemical compositions (Fig. 4b). Thus, the association of Nb-Ta oxides with magmatic micas implies that primary Nb-Ta mineralization was also a magmatic process (Van Lichtervelde et al., 2018).

The mineralization of the Nb-Ta oxides began with primary magmatic crystallization of homogeneous euhedral to subhedral columbite, zoned both within and among crystals from very Nb-rich columbite-(Mn) towards Ta-bearing columbite-(Fe). Later these were overgrown and partly replaced by more Ta-rich columbite-(Mn) as well as hydrothermally-grown fluorcalcomicrolite and wodginite. Experimental data prove that columbite can crystallize from a melt that has MnO + FeO contents >0.05 wt.% and Nb concentrations of ~70-100 ppm at relatively low temperatures, ~600 ^{o}C (Linnen and Keppler, 1997). Experiments also show that fluxes and melt compositions have strong effects on the solubility of tantalum and niobium oxides (e.g., Linnen and Keppler, 1997; Chevychelov et al., 2010; Fiege et al., 2018; Van Lichtervelde et al., 2018; McNeil et al., 2020).

Some columbite crystal cores show normal zoning (Fig. 4k), with smooth and continuously correlated variations in Mn/(Mn+Fe) and Ta/(Ta+Nb), surrounded by a discrete mantle with modestly elevated Ta. Such zoning could conceivably reflect either disequilibrium growth (with delivery of Nb and Ta to the growing crystal limited by sluggish diffusion in the melt) or equilibrium growth (with partitioning controlled by changes in equilibrium conditions and residual melt composition during magmatic fractionation) (Sami et al., 2017). In either case, the trend of correlated increasing Nb/(Nb+Ta) and Mn/(Mn+Fe) seen in the core of the Mueilha columbite is commonly interpreted as a primary magmatic fractionation trend (e.g. Černý et al., 1986) (Fig. 4c). The regularly zoned core is surrounded by a Ta-enriched columbite zone, with some evidence of embayment and resorption of the core that may indicate effects of a late- to post-magmatic, corrosive, supercritical vapour phase.

Finally, most columbite grains are overgrown or partly replaced by very Ta-rich phases, fluorcalciomicrolite and wodginite. These phases always surround remnants of corroded, rounded, or resorbed columbite and are not found as independent crystals. Hydrothermal overprints can cause replacement textures in Nb-Ta oxides (Van Lichtervelde et al., 2007) similar to those observed in backscatter images of the present samples (Fig. 4c). The fluorcalciomicrolite is calcium-dominant but also contains notable levels of sodium and represents the product of interaction between primary Mn and Fe-rich oxides of Nb and post-magmatic hydrothermal fluids with high activity of alkalis and calcium (Atencio et al., 2010).

8. Conclusions

- The post-collisional Mueilha granite intrusion was emplaced into metamorphic country rocks with sharp intrusive contacts. The Mueilha intrusion forms an ellipsoidal intrusive stock covering ~ 7.5 km^2.

- The Mueilha intrusion likely represents a magmatic cupola above highly fractionated A-type magma. The intrusion crystallized under subvolcanic conditions and emplaced a porphyritic phase along the upper contact. Subsequently, the granite magma crystallized inwards from its margins, forming a differentiation series from pinkish-white garnet-bearing granite through red muscovite granite to red alkali feldspar granite.
- The main emplacement mechanism and evolutionary sequence of the Mueilha granites was magmatic, although the effects of hydrothermal fluids and extensive replacement by secondary minerals are observed in an upper marginal zone at the apex of the granitic intrusion. Early stages of hydrous metasomatism are marked by the crystallization of anomalously Mn-rich garnet in the pinkish-white garnet-bearing granite, while extensive alteration and extensive K leaching left a zone of white albite granite.
- The Mueilha granites are highly fractionated with slightly peraluminous character preserved in the fresh red granite. They have many characteristics similar to A-type granites, such as high Ga/Al, Nb, Zr, Y, Ta and Th and significant depletion in MgO, CaO and P_2O_5.
- The Mueilha granites show subparallel chondrite-normalized REE patterns, with enrichment of HREE relative to LREE [$(La/Lu)_n$ = 0.09 to 0.31] and strongly negative Eu anomalies, [(Eu/Eu*)=0.01-0.08].
- Nb-Ta oxides mineralization began with crystallization of normally zoned magmatic euhedral to subhedral columbite, overgrown later by hydrothermal fluorcalciomicrolite and wodginite.

- The whole intrusion appears to have formed in a single magmatic pulse. Magmatic evolution is consistent with simple fractional crystallization, followed by a probably endogenous stage of hydrothermal alteration that produced pegmatite, greisen, quartz and fluorite veins, and the white albite granite cap. The partial melting of juvenile ANS crust to produce the parent magma of Mueilha granites was likely caused by underplating of mantle-derived magma generated during a post-collisional lithospheric delamination process, in the presence of extensional stresses that promoted ascent and emplacement of highly fractionated upper crustal plutons along regional strike-slip faults and shear zones.

Acknowledgments

We acknowledge the National Research Centre, Egypt for supporting this study as a part of the internal project (No. 12010306) of studies of the rare-metal bearing granites in the Eastern Desert of Egypt. This work is a part of the master’s thesis of Amany M.A. Seddik (the first author). FDA is support by the US NSF through award 1550934. The authors highly appreciate thoughtful reviews by the two anonymous reviewers. In addition, the authors are also indebted to the editor (Prof. Michael Roden) for his efforts and numerous helpful comments.

Declaration of Interest Statement

The present work deals the Mueilha intrusion which represents one of the most outstanding example of rare-metal (Ta-Sn-Nb) granite in the Eastern Desert of Egypt, the northwestern corner of the Arabian-Nubian Shield. This work integrates field observations, petrography, mineral chemistry and whole-rock chemical analyses to discern the petrological characteristics of the Mueilha rare-metal granites in order to separate the magmatic and metasomatic stages of evolution of the pluton.

We also aim to better document and understand the alteration zones and the formation of potential associated ore deposits. Also, this study offers a good opportunity to understand the petrogenetic processes leading to the formation of mineralized post-collisional granites throughout the ANS and elsewhere. Therefore, the present work will be interesting for international attentive, in addition to those geoscientists whom studying the Arabian-Nubian Shield in particular.

References

Abdel-Rahman, A.M., 1994. Nature of biotites from alkaline, calc-alkaline and peraluminous magmas. Journal of petrology 35, 525-541.

Abou El Maaty, M.A., Ali Bik, M.W., 2000. Petrology of alkali feldspar granites of Nuweibi and Gebel El-Mueilha, central Eastern Desert, Egypt. Egyptian Journal of Geology 44, 127-148.

Abu El-Rus, M.A., Mohamed, M.A., Lindh, A., 2017. Mueilha rare metals granite, Eastern Desert of Egypt: An example of amagmatic-hydrothermal system in the Arabian-Nubian Shield. Lithos 294–295, 362–382.

Abuamarah, B.A., Azer, M.K., Asimow, P.D., Ghrefat, H., Mubarak, H.S., 2019. Geochemistry and Petrogenesis of late Ediacaran Rare-metal Albite Granites of the Arabian-Nubian Shield. Acta Geologica Sinica (Published online: https://doi.org/10.1111/1755-6724.14379).

Ali, K.A., Moghazi, A.K.M., Maurice, A.E., Omar, S.A., Wang, Q., Wilde, S.A., Moussa, E.M., Manton, W.I., Stern, R.J., 2012. Composition, age, and origin of the ~620 Ma Humr Akarim and Humrat Mukbid A-type granites: no evidence for pre-Neoproterozoic basement in the Eastern Desert, Egypt. International Journal of Earth Sciences 101(7), 1705-1722.

Atencio, D., Andrade, M. B., Christy, A. G., Gieré, R., Kartashov, P. M., 2010. The pyrochlore supergroup of minerals: nomenclature. The Canadian Mineralogist 48, 673-698.

Avigad, D., Gvirtzman, Z., 2009. Late Neoproterozoic rise and fall of the northern Arabian–Nubian shield: the role of lithospheric mantle delamination and subsequent thermal subsidence. Tectonophysics 477, 217–228.

Azer, M.K., Abdelfadil, K.M., Ramadan, A.A., 2019. The Nuweibi rare-metal albite granite: a magmatic cupola above a highly fractionated post-collisional A-type granite pluton. Journal of Geology 127(6), 665–689.

Ballouard, C., Poujol, M., Boulvais, P., Branquet, Y., Tartèse, R., Vigneresse, J.L., 2016. Nb–Ta fractionation in peraluminous granites: a marker of the magmatic-hydrothermal transition. Geology 44, 231–234.

Batchelor, R.A., Bowden, P., 1985. Petrogenetic interpretation of granitoid rock series using multicationic parameters. Chemical Geology 48, 43-45.

Be'eri-Shlevin, Y., Samuel, M.D., Azer, M.K., Rämö, O.T., Whitehouse, M.J., Moussa, H.E., 2011. The late Neoproterozoic Ferani and Rutig volcano-sedimentary successions of the northernmost Arabian-Nubian Shield (ANS): New insights from zircon U-Pb geochronology, geochemistry and O-Nd isotope ratios. Precambrian Research 188, 21-44.

Beus, A.A., 1982. Metallogeny of Precambrian rare-metal granitoids. Revista Brasileira de Geociências 12, 410-413.

Black, R., Lameyre, J., Bonin, B., 1985. The structural setting of alkaline complexes. Journal of African Earth Sciences 3(1-2), 5-16.

Blasband, B., White, S., Brooijmans, P., De Broorder, H., Visser, W., 2000. Late Proterozoic extensional collapse in the Arabian-Nubian Shield. Journal of Geological Society of London 157, 615-628.

Bonin, B., 2007. A-type granites and related rocks: Evolution of a concept, problems and prospects. Lithos 97, 1-29.

Černý, P., Goad, B.E., Hawthorne, F.C., Chapman, R., 1986. Fractionation trends of the Nb-and Ta-bearing oxide minerals in the Green Lake pegmatitic granite and its pegmatite aureole, southeastern Manitoba. American Mineralogist, 71(3-4), pp.501-517.

Chevychelov, V.Y., Borodulin, G.P., Zaraisky, G.P., 2010. Solubility of columbite, (Mn, Fe)(Nb, Ta)$_2$O$_6$, in granitoid and alkaline melts at 650–850° C and 30–400 MPa: An experimental investigation. Geochemistry International 48(5), 456-464.

Chevychelov, V.Y., Zaraisky, G.P., Borisovskii, S.E., Borkov, D.A., 2005. Effect of melt composition and temperature on the partitioning of Ta, Nb, Mn, and F between granitic (alkaline) melt and fluorine-bearing aqueous fluid: fractionation of Ta and Nb and conditions of ore formation in rare-metal granites. Petrology c/c of Petrologiia 13(4), p. 305.

Clemens, J.D., Holloway, J.R., White, A.J.R., 1986. Origin of an A-type granites: experimental constraints. American Mineralogist 71, 317-324.

Cuney, M., Marignac, C., Weisbrod, A., 1992. The Beauvoir topaz-lepidolite albite granite (Massif Central France): the disseminated magmatic Sn–Li–Ta–Nb–Be mineralization. Economic Geology 87, 1766–1794.

Dahlquist, J. A., Galindo, C., Pankhurst, R. J., Rapela, C. W., Alasino, P. H., Saavedra, J., Fanning, C. M., 2007. Magmatic evolution of the Peñón Rosado granite: Petrogenesis of garnet-bearing granitoids. Lithos 95, 177-207.

De la Roche, H., Leterrier, J., Grandclaude, P., Marchal, M., 1980.A classification of volcanic and plutonic rocks using R_1-R_2 diagrams and major-element analyses-Its relation with current nomenclature. Chemical Geology 29, 183-210.

Eby, G.N., 1992. Chemical subdivisions of the A-type granitoids: petrogenesis and tectonic implications. Geology 20, 641-644.

El-Galy, M.M., Khaleal, F.M., Bakhit, A.M., 2016. Comparative study on the geological and geochemical characteristics of some rare-metal granites, southeastern desert, Egypt. Nuclear Sciences Scientific Journal 5(1), 109-120.

El-Sayed, M.M., Mohamed, F.H., Furnes, H., Kanisawa, S., 2002. Geochemistry and petrogenesis of the Neoproterozoic granitoids in the central eastern desert, Egypt. Chemie der Erde 62, 317-346.

Evensen, N.M., Hamilton, P.J., O' Nions, R.K., 1978. Rare earth abundances in chondritic meteorites. Geochimica et Cosmochimica Acta 42(8), 1199-1212.

Eyal, M., Litvinovsky, B., Jahn, B.M., Zanvilevich, A., Katzir Y., 2010. Origin and evolution of post-collisional magmatism: Coeval Neoproterozoic calc-alkaline and alkaline suites of the Sinai Peninsula. Chemical Geology 269, 153-179.

Farahat, E.S., Mohamed, H.A., Ahmed, A.F., El Mahallawi, M.M. 2007. Origin of I- and A-type granitoids from the Eastern Desert of Egypt: implications for crustal growth in the northern Arabian–Nubian Shield. Journal of African Earth Science 49, 43-58.

Fiege, A., Simon, A., Linsler, S.A., Bartels, A., Linnen, R.L., 2018. Experimental constraints on the effect of phosphorous and boron on Nb and Ta ore formation. Ore Geology Reviews 94, 383-395.

Frost, B.R., Barnes, C.G., Collins, W.J., Arculus, R.J., Ellis, D.J., Frost, C.D., 2001. A geochemical classification for granitic rocks. Journal of Petrology 42, 2033-2048.

Harris, N.B., Pearce, J.A., Tindle, A.G., 1986. Geochemical characteristics of collision-zone magmatism. In: Coward, M.P., Ries, A.C. (Eds.), Collision Tectonics. Journal of Geological Society, London, Special Publication 19, pp. 67–81.

Hassanen, M.A., Saad, N.A., Khalifa, O.M., 1995. Geochemical aspects and origin of Tin-bearing granites in the Eastern Desert, Egypt. Acta Mineralogica-Petrographica XXXVI, 55-72.

Heikal, M.T.S., Khedr, M.Z., El-Monesf, M.A. and Gomaa, S.R., 2019. Petrogenesis and geodynamic evolution of Neoproterozoic Abu Dabbab Albite Granite, Central Eastern Desert of Egypt: Petrological and geochemical constraints. Journal of African Earth Sciences 158, 103518.

Helba, H., Trumbull, R.B., Morteani, G., Khalil, S.O., Arslan, A., 1997. Geochemical and petrographic studies of Ta mineralization in the Nuweibi albite granite complex, Eastern Desert, Egypt. Mineralium Deposita 32(2), 164–179.

Holtz, F., Behrens, H., Dingwell, D.B., Taylor, R.P., 1992. Water solubility in aluminosilicate melts of haplogranite composition at 2 kbar. Chemical Geology 96, 289-302.

Jahn, S., 1996. Geochemische und mineralogische Untersuchungen zur Metallogenese Seltenmetall-führen der Granitoide in der Central Eastern Desert, Ägypten. Unpubl. Ph.D thesis, Technische Universität Berlin, 271 pp.

Liégeois, J.P., Navez, J., Black, R., Hertogen, J., 1998. Contrasting origin of post-collision high-K calc-alkaline and shoshonitic versus alkaline and peralkaline granitoids. The use of sliding normalization. Lithos 45, 1-28.

Linnen, R.L., Keppler, H., 1997. Columbite solubility in granitic melts: consequences for the enrichment and fractionation of Nb and Ta in the Earth's crust. Contributions to Mineralogy and Petrology, 128(2-3), pp.213-227.

London, D., 2015. Reading pegmatites: Part 1—What beryl says. Rocks and Minerals 90(2), 138-153.

Lundstrom, C.C., 2016. The role of thermal migration and low-temperature melt in granitoid formation: can granite form without rhyolitic melt? International Geology Review 58(3), 371-388.

Maniar, P.D., Piccoli, P.M., 1989. Tectonic discrimination of granitoids. Geological society of America Bulletin 101(5), 635-643.

Manning, D.A.C., 1981. The effect of fluorine on liquidus phase relationships in the system Qz–Ab–Or with excess water at 1 kb. Contributions to Mineralogy and Petrology 76, 206–215.

McNeil, A.G., Linnen, R.L., Flemming, R.L., 2020. Solubility of wodginite, titanowodginite, microlite, pyrochlore, columbite-(Mn) and tantalite-(Mn) in flux-rich haplogranitic melts between 700° and 850° C and 200 MPa. Lithos 352, 105239.

Miller, C.F., Stoddard, E.F., 1981. The role of manganese in the paragenesis of magmatic garnet: an example from the Old Woman-Piute Range, California. The Journal of Geology 89, 233–246.

Miller, C.F., Stoddard, E.F., Bradfish, L.J., Dollase, W.A., 1981. Composition of plutonic muscovite: genetic implications. Canadian Mineralogist 19(1), 25-34.

Mohamed, F.H., 1993. Rare-metal-bearing and barren granites, Eastern Desert of Egypt: geochemical characterization and metallogenetic aspects. Journal of African Earth Sciences 17, 525-539.

Mohamed, M.A.M., 2013. Evolution of mineralizing fluids of cassiterite–wolframite and fluorite deposits from Mueilha tin mine area, Eastern Desert of Egypt, evidence from fluid inclusion. Arabian Journal of Geosciences 6(3), 775-782.

Montel, J.M., Vielzeuf, D., 1997. Partial melting of metagreywackes, Part II. Compositions of minerals and melts. Contribution to Mineralogy and Petrology 128, 176-196.

Morsy M.A., Mohamed, F.H., 1992. Geochemical characteristics and petrogenetic aspects of Mueilha tin-specialized granite, Eastern Desert, Egypt. Bulletin of Faculty of Science, Alexandria University, Egypt 32(A), 502–515.

Müller, A., Seltmann, R., 1999. The genetic significance of snowball quartz in high fractionated tin granites of the Krušne Hory/Erzgebirge. Mineral deposits: processes to processing 1, 409-412.

Nachit, H., Razafimahefa, N., Stussi, J.M., Carron, J.P., 1985. Composition chimique des biotites et typologie magmatique des granitoides. Comptes Rendus Hebdomadaires de l'Academie des Sciences 301(11), 813-818.

Nachit, H., Ibhi, A. and Ohoud, M.B., 2005. Discrimination between primary magmatic biotites, reequilibrated biotites and neoformed biotites. Comptes Rendus Geoscience, 337(16), pp.1415-1420.

Nurmi, P.A., Haapala, I., 1986. The Proterozoic granitoids of Finland: granite types, metallogeny and relation to crustal evolution. Bulletin of the Geological Society of Finland 58, 203-233.

Patiño Douce, A.E., 1999. What do experiments tell us about the relative contributions of crust and mantle to the origin of granitic magmas? In: Castro, A., Fernandez, C. &Vigneresse, J. (eds) Understanding Granites: Integrating New and Classical Techniques. Geological Society, London, Special Publications 168, 55–75.

Pearce, J.A., 1983. Role of the sub-continental lithosphere in magma genesis at active continental margins. In Continental Basalts and Mantle Xenoliths. In: Hawkesworth, C.J.and Norry, M.J. (Eds.). Shiva Press, Nantwich, U.K., 230-249.

Pearce, J.A., Harris, N.B.W., Tindle, A.G., 1984. Trace element discrimination diagrams for the tectonic interpretation of granitic rocks. Journal of Petrology 25, 956-983.

Richard, L.R., 1995. Mineralogical and petrological data processing system. Minpet Software (c) 1988-1995, Version 2.02.

Salem, A. K. A., Kabesh, M. L., Ghazaly, M., 1985. Petrochemistry, petrogenesis and classification of Um Huqab, Garf and El-Mueilha granitic masses, Southeastern Desert, Egypt. Mineralogica-Petrographica, XXVII, 17-31.

Sami, M., Ntaflos, T., Farahat, E.S., Mohamed, H.A., Ahmed, A.F., Hauzenberger, C., 2017. Mineralogical, geochemical and Sr-Nd isotopes characteristics of fluorite-bearing granites in the Northern Arabian-Nubian Shield, Egypt: Constraints on petrogenesis and evolution of their associated rare metal mineralization. Ore Geology Reviews 88, 1-22.

Sami, M., Ntaflos, T., Farahat, E.S., Mohamed, H.A., Hauzenberger, C., Ahmed, A.F., 2018. Petrogenesis and geodynamic implications of Ediacaran highly fractionated A-type granitoids in the north Arabian-Nubian Shield (Egypt): Constraints from whole-rock geochemistry and Sr-Nd isotopes. Lithos 304, 329-346.

Schmitz, C., Burt, D.M., 1990. The Black Pearl mine, Arizona: Wolframite veins and stockscheider pegmatite related to an albitic stock. Special Paper - Geological Society of America 246, 221–232.

Smirnov, V.I., Ginzburg, A.I., Grigoriev, V.M. and Yakovlev, G.F. (1983) Studies of Mineral Deposits. Mir Pub., Moscow.

Stern, R.J., 1994. Arc assembly and continental collision in the Neoproterozoic East African Orogen: implications for the consolidation of Gondwanaland. Annual Reviews of Earth and Planetary Science 22, 319-351.

Stern, R.J., Hedge, C.E., 1985. Geochronologic constraints on late Precambrian crustal evolution in the Eastern Desert of Egypt. American Journal of Science 285, 97–127.

Stoeser, D.B., Frost, C.D., 2006. Nd, Pb, Sr, and O isotopic characterization of Saudi Arabian Shield terranes. Chemical Geology 226, 163-188.

Streckeisen, A., Le Maitre, R.W., 1979. A chemical approximation to the modal QAPF classification of igneous rocks. Neues Jahrbuch für Mineralogie Abh 136,169-206.

Sun, S., McDonough, W.F., 1989. Chemical and isotopic systematic of oceanic basalts: implications for mantle compositions and processes. Magmatism in the Ocean Basins: In: Saunders AD, Norry MJ (eds.), Geological Society of London, Special Publications 42, 313-345.

Sylvester, P.J., 1989. Post-collisional alkaline granites. Journal of Geology 97(3), 261-280.

Tollo, R.P., Aleinikoff, J.N., Bartholomew, M.J., Rankin, D.W., 2004. Neoproterozoic A-type granitoids of the central and southern Appalachians: intraplate magmatism associated with episodic rifting of the Rodinian supercontinent. Precambrian Research 128, 3-38.

Turner, S.P., Foden, J.D., Morrison, R.S., 1992. Derivation of some A-type magmas by fractionation of basaltic magma—an example from the Padthaway Ridge, South Australia. Lithos 28, 151-179.

Van Lichtervelde, M., Holtz, F., Melcher, F., 2018. The effect of disequilibrium crystallization on Nb-Ta fractionation in pegmatites: Constraints from crystallization experiments of tantalite-tapiolite. American Mineralogist 103(9), 1401-1416.

Van Lichtervelde, M., Salvi, S., Beziat, D., Linnen, R.L., 2007. Textural features and chemical evolution in tantalum oxides: magmatic versus hydrothermal origins for Ta mineralization in the Tanco Lower Pegmatite, Manitoba, Canada. Economic Geology 102(2), 257-276.

Vance, J.A., 1969. On Synneusis. Contributions to Mineralogy and Petrology 24, 7-29.

Wang, R.C., Wu, F.Y., Xie, L., Liu, X.C., Wang, J.M., Yang, L., Lai, W., Liu, C., 2017. A preliminary study of rare-metal mineralization in the Himalayan leucogranite belts, South Tibet. Science China Earth Sciences 60, 1655–1663.

Whalen, J.B., Currie, K.L., Chappell, B.W., 1987. A-type granites: geochemical characteristics, discrimination and petrogenesis. Contribution to Mineralogy and Petrology 95(4), 407-419.

Whitworth, M.P., 1992. Petrogenetic implications of garnets associated with lithium pegmatites from SE Ireland. Mineralogical Magazine 56, 75–85.

Winkler, H.G.F., Boese, M., Marcopoulos, T., 1975. Low temperature granite melts. Neues Jahrbuch für Mineralogie. Monatshefte 6, 245–268.

Wu, F.-Y., Sun, D.-y., Li, H., Jahn, B.-m., Wilde, S., 2002. A-type granites in northeastern China: age and geochemical constraints on their petrogenesis. Chemical Geology 187, 143–173.

Zen, E.A., 1988. Phase relations of peraluminous granitic rocks and their petrogenetic implications. Annual Review of Earth and Planetary Sciences 16, 21-51.

Zhang, J., Ma, C., She, Z., 2012. An Early Cretaceous garnet-bearing metaluminous A-type granite intrusion in the East Qinling Orogen, central China: petrological, mineralogical and geochemical constraints. Geoscience Frontiers 3, 636–646.

Figure 1. (a) General geologic map of the central and southern sectors (dividing line after Stern and Hedge, 1985) of the Eastern Desert of Egypt showing the locations of the most important rare-metal bearing granite intrusions: (1) Umm Naggat, (2) Umm Samra, (3) Abu Dabbab, (4) Nuweibi, (5) Ineiga, (6) Homrit Waggat, (7) Igla, (8) Zabara, (9) Mueilha, (10) Nugrus, (11) El-Gharabiya, (12) Nikeiba, (13) Homrit Akarem, and (14) Um Ara. (b) Satellite image (Google Earth) of the Mueilha area showing the topographic expression of the Mueilha granite intrusion (light color) into dark metasedimentary rocks. (c) Geologic map of the Mueilha area (after Abu El-Rus et al., 2017). (d) Schematic cross-section (no vertical exaggeration) showing the field relationships between the different rock types of the Mueilha intrusion and their country rocks. Note line of section marked on Figure 1c.

Figure 2. Field photographs of the Mueilha intrusion. (a) and (b) Sharp intrusive contacts between the Mueilha intrusion and its metamorphic country rocks. (c) Apophysis of the Mueilha granite into the adjacent metasediments. (d) Small diapir of Mueilha granite piercing the country rock. (e) Sharp intrusive contact between the red and white granites. (f) Roof pendant of the white granite above the red granite.

Figure 3. Hand specimens of the rock types in the Mueilha intrusion: (a) alkali feldspar granite, (b) muscovite granite, (c) garnet-bearing granite, and (d) albite granite.

Figure 4. Key petrographic features (a, b, d, f, i and j in cross-polarized transmitted light; g in plane-polarized transmitted light; c, e, h, k and l in back-scattered electron images). (a) Plagioclase inclusion within perthite crystal. (b) Inclusion of zircon and secondary muscovite veinlet within quartz. (c) Overgrowth and partial replacement of zoned columbite by late Ta-rich oxide phases. (d) Tabular crystal of primary muscovite with high interference color. (e) Fine anhedral crystals of Nb-Ta oxides included in feldspars. (f) Myrmekitic intergrowth between quartz and K-feldspar. (g) Fractured garnet crystals surrounded by reaction rims of altered chlorite. (h) Corroded crystal of Nb-Ta oxide. (i) Snowball texture of albite laths within quartz. (j) Corroded muscovite within K-feldspar. (k) Tabular columbite crystal with spotted Ta-enriched margins, associated with biotite. (l) Homogeneous tabular columbite crystal with normal zoning, interstitial among feldspar crystals.

Figure 5. Mineral chemistry of Mueilha intrusion samples. **(**a) Compositional fields for primary and secondary muscovite in the ternary diagram of Miller et al. (1981). (b) TiO_2-($FeO_{(t)}$+MnO)-MgO ternary diagram for classification of biotite (after Nachit et al. 2005). (c) $FeO_{(t)}$ vs. Al_2O_3 discrimination diagram for biotite (Abdel-Rahman, 1994).(d) Mg vs. Al discrimination diagram for biotite (Nachit et al., 1985).(e) Chemical composition and nomenclature of the columbite-tantalite group minerals based on Ta/(Ta+Nb) vs. Mn/(Mn+Fe) ratios. (f) Mn-Mg-Fe ternary discrimination diagram for garnet (Miller and Stoddard, 1981).

Figure 6. Whole-rock major element chemistry. (a) Nomenclature of the plutonic rocks using the R_1-R_2 diagram (De la Roche et al., 1980).(b) $Q^/(F^/)$-ANOR diagram for normative classification of granitoids (Streckeisen and Le Maitre, 1979); $Q^/$=100*Q/(Q+Or+Ab+An); $F^/$= (Ne+Lc+Kp)/(Ne+Lc+Kp+Or+Ab+An); ANOR=100*An/(Or+An).

Figure 7. Variation diagrams of some major oxides against SiO_2. Symbols as shown in the legend of Fig. 5.

Figure 8. Variation diagrams of some whole-rock trace elements against SiO_2. (a) Six panels showing trace elements that positively correlate with SiO_2. (b) Eight panels showing trace elements that negatively correlate with SiO_2. Symbols as shown in the legend of Fig. 5.

Figure 9. Normalized multi-trace element diagrams for whole-rock chemistry. (a) Mid-ocean ridge basalt (MORB)-normalized extended trace element diagram; MORB normalization values from Sun and McDonough (1989). (b) Chondrite-normalized REE patterns; chondrite values from Evensen et al. (1978). Symbols as shown in the legend of Fig. 5.

Figure 10. Classification diagrams based on whole-rock chemistry. (a) $(Al_2O_3+CaO)/(FeO_{(t)}+Na_2O+K_2O)$ versus $100*(MgO+FeO_{(t)}+TiO_2)/SiO_2$ for distinguishing between calc-alkaline, highly fractionated calc-alkaline, and alkaline granite (Sylvester,

1989). (b) $Al_2O_3/(Na_2O+K_2O)$ versus $Al_2O_3/(CaO+Na_2O+K_2O_3)$ for granitoid rocks (after Maniar and Piccoli, 1989). (c) Ga/Al against $FeO_{(t)}/MgO$ for distinguishing between I, S, M and A-type granites (Whalen et al., 1987). (d) Chemical classification diagram using SiO_2 versus Na_2O+K_2O-CaO (Frost et al., 2001). (e) FeO-10*MgO-MnO ternary discrimination diagram for garnet; the fields of different granites are from Zhang et al. (2012). (f) Rb/Nb versus Y/Nb diagram (Eby, 1992) to distinguish between A_1 and A_2 granitoids; A_1 are anorogenic A-type granites with mantle signatures whereas A_2 are post-collisional A-type granites with crustal sources. Symbols as shown in the legend of Fig. 5.

Figure 11. Further tectonic discrimination diagrams based on whole-rock trace-element chemistry. (a) Nb vs. Y diagram (Pearce et al., 1984).. (b) R_1-R_2 multicationic diagram (Batchelor and Bowden,1985), (c) Hf-Rb/30-3*Ta ternary diagram (after Harris et al., 1986). Abbrevations: R_1=4Si-11(Na+K)-2(Fe+Ti); R_2=6Ca+2Mg+Al; VAG: volcanic-arc granites; syn-COLG: syn-collisional granites; WPG: within-pate granites; ORG: ocean-ridge granites. Symbols as shown in the legend of Fig. 5.

Figure 12. Simplified model for the geodynamic evolution of the post-collisional Mueilha intrusion showing lithospheric delamination, upwelling of asthenospheric mantle, generation of underplated basic magma, partial melting of lower and middle crust, generation of A-type granitic magma, emplacement of highly-fractionated magma extending to subvolcanic levels, and finally erosional removed of cover to explore the top of the pluton. Processes not shown in this two-dimensional section include

cessation of collision and slab breakoff at the beginning of the cycle or tilting of the pluton to expose a depth section at the end.

Figure 13. (a) Normative composition of the Mueilha granites plotted in Qz–Ab–Or projection. Dashed lines show quartz-alkali feldspar cotectics and the trace of the water-saturated minimum melt compositions in the haplogranite system at total pressure ranging from 0.5 to 10 kbar (Holtz et al., 1992; Winkler et al., 1975). Solid line shows the trace of the minimum melt composition at 1 kbar with excess H_2O and increasing fluorine (F) content up to 4 wt.% F (Manning, 1981). (b) Rb/Sr versus Sr diagram. Symbols as shown in the legend of Fig. 5.

Table 1. Major oxide and trace element contents of the Mueilha granites, Eastern Desert, Egypt.

Rock type	Alkali feldspar granite			Muscovit granite					Garnet bearing granite		Albite granite				
Sample No	MH0	MH 1a	MH 1b	MH 2	MH 3	MH 4a	MH 4b	MH 5	MH10	MH14	MH6	MH 7	MH 8	MH 9	MH 11
Major oxides (wt.%)															
SiO2	78.35	76.63	76.04	76.5	74.19	75.13	75.18	74.7	73.29	71.89	73.63	74.43	73.89	74.29	73.14
TiO2	0.01	0.02	0.01	0.02	0.0[illegible]	0.01	0.02	0.02	0.02	0.04	0.04	0.03	0.03	0.02	0.03
Al2O3	12.1	13.23	13.19	13.11	14.77	14.29	14.14	14.4	15.13	15.08	14.74	14.38	14.57	14.8	15.11
Fe2O3	0.44	0.46	0.48	0.45	0.47	0.45	0.47	0.45	0.45	0.46	0.43	0.44	0.42	0.43	0.46
MnO	0.04	0.03	0.04	0.02	0.04	0.04	0.04	0.03	0.03	0.05	0.02	0.03	0.03	0.02	0.04
MgO	0.02	0.01	0.01	0.02	0.01	<dl	0.02	0.01	0.03	0.04	<dl	<dl	0.01	0.02	0.02
CaO	0.26	0.31	0.28	0.27	0.3	0.28	0.26	0.34	0.35	0.44	0.33	0.34	0.36	0.32	0.38
Na2O	4.12	4.78	4.85	4.9	4.92	4.81	4.68	4.59	6.76	7.41	6.64	6.54	5.95	5.52	7.16
K2O	4.28	3.72	3.91	3.87	3.85	4.02	4	4.05	3.42	3.87	3.99	3.21	3.84	3.78	3.26
P2O5	0.01	0.01	0.02	0.01	0.01	0.01	0.03	0.01	0.01	0.01	<dl	<dl	<dl	<dl	0.01
LOI	0.47	0.26	0.25	0.28	0.34	0.35	0.3	0.42	0.25	0.28	0.27	0.21	0.3	0.34	0.33
Total	100.21	99.42	99.13	99.47	98.91	99.39	99.12	99.03	99.7	99.57	100.19	99.75	99.43	99.42	99.99
Trace elements (ppm)															
Rb	543.1	498.2	452.5	494.6	455.8	465.3	476.3	455.7	436.2	401.3	390.3	405.6	428.1	431.6	409.5

Ba	15.8	14.4	17.5	11.5	19.6	8.3	12.3	11.2	20.5	29.7	17.5	19.1	24.5	26.3	24.2
Sr	11.3	12.5	10.5	13	15.6	12.4	13.5	14.7	15.4	21.5	13.5	19.4	16.9	17.6	16.2
Nb	69.8	68.5	74.4	71.3	66.4	54.7	61.8	59.3	64.4	54.6	56.7	52.4	30.5	67.2	61.5
Zr	59.1	70.3	78.8	66.3	72.4	71.8	77.7	85.4	43.5	43.4	58.9	64.1	58.2	58.6	49.7
Hf	8.3	7.5	8.6	6.1	7.8	8.1	8.5	8.8	6.5	7.4	6.2	7	6	6.7	7.6
Y	87.6	77.6	89.5	73	83.4	78.2	76.5	81.3	29.4	17.6	36.3	35.9	54.4	40.9	15.4
Zn	98.4	86.9	107.1	82.5	91.7	75.6	101.5	80.9	27.3	26.4	15.3	37.7	42.3	70.5	24.5
Cu	2.5	3.3	2.2	2.8	2.8	3.6	2.5	3.2	4.7	5.2	3.2	3.1	3.7	4.2	5.5
Ni	3.3	3.5	3.1	2.9	4.3	5.6	5	4.3	5.9	8.1	7.2	6.4	5.1	6.4	6.3
Cr	10.6	14.3	13.5	12.1	16.5	9.8	14.2	13.1	18.6	20.7	16.8	17.3	17.6	18	19.2
V	1.4	<dl	2.2	<dl	1.7	<dl	2.7	1.8	2.4	3.9	2.2	1.9	2.1	2.1	2.7
Pb	24.3	21	17.5	23.5	18.6	27.6	22.5	21.7	25.7	20.5	27.9	31.2	30.3	21	22.6
Sc	0.5	0.6	0.5	0.7	0.8	0.7	0.6	0.7	1.1	1.2	0.7	0.9	1.1	1	0.9
Ta	24.8	23.3	18.8	16.3	15.4	18.1	21.8	19.3	21.4	19.2	17.9	23.1	23.48	22.7	24.3
W	0.5	0.7	0.5	0.4	0.3	0.6	0.4	0.3	0.3	0.3	0.5	0.2	0.7	0.4	0.4
Th	21.2	23.5	24.5	18.5	19.6	22.7	20.4	21.5	17.6	15.7	18.4	17.1	17.1	19.1	16.4
U	12.2	11.8	10.1	13.5	9.4	6.8	8.1	9.7	5.6	4.5	4.4	5.4	4.9	6.1	6.2
Ga	29.5	32.7	31.8	33.6	37.5	36.9	39.1	4[illegible].1	48.7	52.8	47.3	46.3	50.6	46.8	54.4
Sn	202.1	139.4	191.8	117.5	200.4	126.3	87.9	90.4	126.4	137.2	76.7	91.1	125.8	133.2	110.9
<u>Geochemical parameters</u>															
AI	0.94	0.90	0.93	0.94	0.83	0.86	0.85	0.83	0.98	1.09	1.03	0.99	0.96	0.89	1.01
ASI	1.02	1.06	1.04	1.03	1.15	1.12	1.13	1.15	0.98	0.88	0.93	0.97	1.00	1.08	0.94
CIA	50.43	51.49	50.88	50.69	53.54	52.78	53.05	53.40	49.44	46.73	48.18	49.18	49.93	51.81	48.56

AI = molar (Na+K)/Al

ASI= molar Al/(Ca+Na+K)

CIA = molecular [Al/(Al+Ca+Na+K)]*100

Table 2. CIPW norm compostions of the Mueilha granites, Eastern Desert, Egypt.

Rock type	Alkali feldspar granite			Muscovite granite					Garnet bearing granite		Albite granite				
Sample No.	MH 0	MH 1a	MH 1b	MH 2	MH 3	MH 4a	MH 4b	MH 5	MH10	MH14	MH 6	MH 7	MH 8	MH 9	MH 11
Quartz	37.32	33.95	32.4	32.63	30.37	31.22	32.25	31.98	20.14	17.04	20.58	23.55	23.8	26.98	15.33
Corundum	0.24	0.8	0.52	0.39	2.01	1.55	1.73	1.89	-	-	-	-	-	1.05	-
Orthoclase	25.39	22.17	23.39	23.07	23.09	23.99	23.92	24.28	20.32	23.04	23.63	19.09	22.91	22.52	18.6
Albite	35	40.79	41.54	41.82	42.25	41.11	40.08	39.4	57.51	56.41	53.69	55.69	50.82	47.1	57.47
Anorthite	1.23	1.49	1.27	1.29	1.44	1.34	1.11	1.65	0.83	0	0	0.39	1.71	1.6	0
Acmite	-	-	-	-	-	-	-	-	-	0.24	0.21	-	-	-	0.89
Na-Metasilicat	-	-	-	-	-	-	-	-	-	1.51	0.55	-	-	-	-

e															
Diopside	-	-	-	-	-	-	-	-	0.75	1.86	1.46	1.17	0.08	-	1.56
Hypersthene	0.65	0.62	0.68	0.62	0.65	0.62	0.68	0.61	0.27	-	-	-	0.51	0.59	5.47
Magnetite	0.11	0.11	0.12	0.11	0.12	0.11	0.12	0.11	0.11	-	-	0.11	0.11	0.1	0.59
Ilmenite	0.02	0.04	0.02	0.04	0.04	0.02	0.04	0.04	0.04	0.08	0.08	0.06	0.06	0.04	0.06
Apatite	0.02	0.02	0.04	0.02	0.02	0.02	0.07	0.02	0.02	0.02	-	-	-	-	0.02
Colour Index	0.78	0.77	0.82	0.77	0.81	0.75	0.83	0.76	1.16	1.72	1.32	1.26	0.75	0.74	7.68
Diff. Index	97.72	96.9	97.33	97.52	95.7	96.33	96.25	95.66	97.97	96.49	97.9	98.33	97.53	96.6	91.4
ANOR	4.62	6.30	5.15	5.30	5.87	5.29	4.43	6.36	3.92	0.00	0.00	2.00	6.95	6.63	0.00
Q	37.72	34.50	32.86	33.02	31.26	31.97	33.12	32.86	20.38	17.06	21.02	23.86	23.98	27.47	16.77

Table 3. Rare earth element contents of the Mueilha granites, Eastern Desert, Egypt.

Rock type	Alkali feldspar granite			Muscovite granite					Garnet bearing granite		Albite granite				
Sample No	MH0	MH1a	MH1b	MH2	MH3	MH4a	MH4b	MH5	MH10	MH14	MH6	MH7	MH8	MH9	MH11
La	10.73	9.18	12.8	5.89	5.43	6.77	4.46	6.26	4.18	3.76	2.85	1.62	1.97	2.42	4.11
Ce	30.77	23.15	37.07	26.27	20.69	21.84	[illegible]	21.25	17.24	15	12.94	9.29	11.7	11.14	14.74
Pr	4.46	3.88	5.31	2.61	2.16	2.99	1.85	2.51	2.33	1.8	2.12	1.64	2.1	1.59	1.78
Nd	17.95	15.27	19.92	9.45	8.61	11.52	6.75	9.38	6.27	4.44	4.97	4.42	5.39	4.06	4.61
Sm	6.72	5.87	7.31	3.47	[illegible]	4.29	2.48	3.71	2.91	1.92	2.55	2.45	2.84	2.32	2.04
Eu	0.01	0.02	0.03	0.02	0.01	0.03	0.03	0.02	0.02	0.04	0.04	0.03	0.04	0.03	0.02
Gd	7.56	6.81	7.85	4.18	4.42	4.72	3.02	4.51	2.13	1.35	0.98	0.9	1.17	1.06	1.35
Tb	1.94	1.76	2.17	1.19	1.24	1.25	1.09	1.32	0.73	0.53	0.49	0.42	0.54	0.45	0.5
Dy	14.74	12.69	16.91	9.5	10.63	9.33	8.42	11.07	5.14	4.13	4.36	3.71	4.69	4.16	3.83
Ho	3.46	3	4.05	2.33	2.71	2.24	2.25	2.85	1.33	0.83	0.85	0.73	0.89	0.87	0.78
Er	13.08	10.51	15.46	9.36	10.76	8.45	8.96	11.19	5.47	3.83	3.66	3.05	3.77	3.95	3.48
Tm	2.83	2.25	3.38	2.14	2.35	1.92	2.07	2.45	1.53	1.2	1.18	0.98	1.25	1.28	0.99
Yb	23.52	18.96	27.77	17.77	19.41	16.05	17.1	20.24	14.08	12.08	12.76	10.78	13.57	13.77	10.71
Lu	3.82	3.06	4.47	2.95	3.08	2.61	2.75	3.22	2.57	1.95	1.93	1.81	2.17	2.46	1.77
Eu/EU*	0.00	0.01	0.01	0.02	0.01	0.02	0.03	0.01	0.02	0.08	0.08	0.06	0.07	0.06	0.04
(La/Yb)n	0.31	0.33	0.31	0.22	0.19	0.29	0.18	0.21	0.20	0.21	0.15	0.10	0.10	0.12	0.26

((La/Sm)n	1.01	0.99	1.11	1.07	1.01	1.00	1.14	1.06	0.91	1.24	0.71	0.42	0.44	0.66	1.27
(Gd/Lu)n	0.24	0.27	0.22	0.17	0.18	0.22	0.13	0.17	0.10	0.08	0.06	0.06	0.07	0.05	0.09
(La/Lu)n	0.29	0.31	0.29	0.20	0.18	0.27	0.17	0.20	0.17	0.20	0.15	0.09	0.09	0.10	0.24

Graphical abstract:

Highlights:

- The Mueilha intrusion was emplaced as a high-level magmatic cupola
- The geochemistry of the Mueilha granites is typical of rare-metal granites
- They are weakly peraluminous and highly fractionated with A-type character
- The Mueilha granites are evolved through a transitional magmatic–hydrothermal stage The primary magma was generated by partial melting of the juvenile continental crust

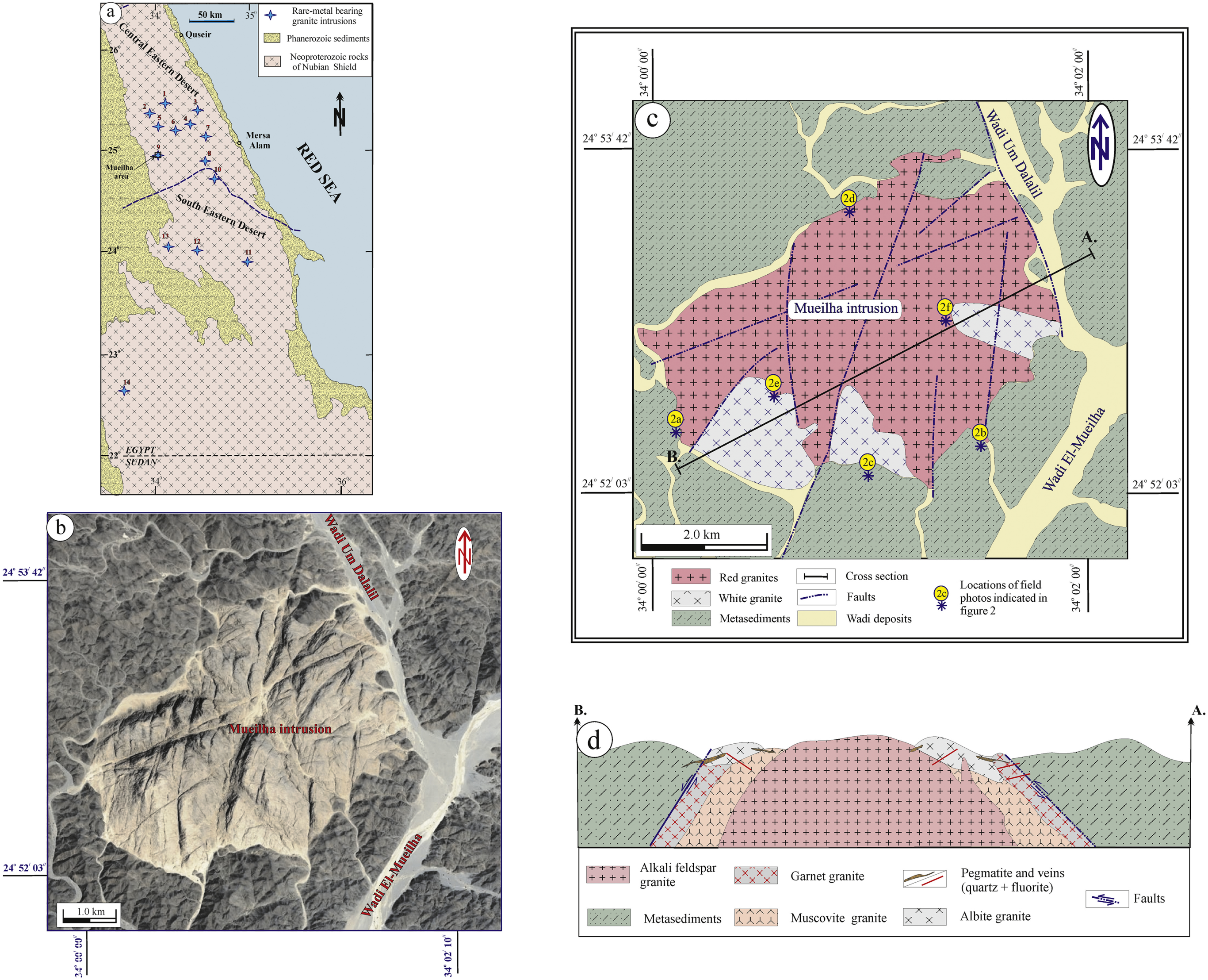
a
50 km
34°
35°
Quseir
26°
25°
24°
23°
22°
Central Eastern Desert
South Eastern Desert
Mersa Alam
RED SEA
Mueilha area
EGYPT
SUDAN
36°
1
2
3
4
5
6
7
8
9
10
11
12
13
14
N
Rare-metal bearing granite intrusions
Phanerozoic sediments
Neoproterozoic rocks of Nubian Shield
b
Wadi Um Dalalil
Wadi El-Mueilha
Mueilha intrusion
1.0 km
24° 53′ 42″
24° 52′ 03″
34° 00′ 00″
34° 02′ 10″
c
34° 00′ 00″
34° 02′ 00″
24° 53′ 42″
24° 52′ 03″
Wadi Um Dalalil
Wadi El-Mueilha
Mueilha intrusion
A.
B.
2a
2b
2c
2d
2e
2f
2.0 km
Red granites
White granite
Metasediments
Cross section
Faults
Wadi deposits
Locations of field photos indicated in figure 2
d
B.
A.
Alkali feldspar granite
Metasediments
Garnet granite
Muscovite granite
Pegmatite and veins (quartz + fluorite)
Albite granite
Faults

Figure 1

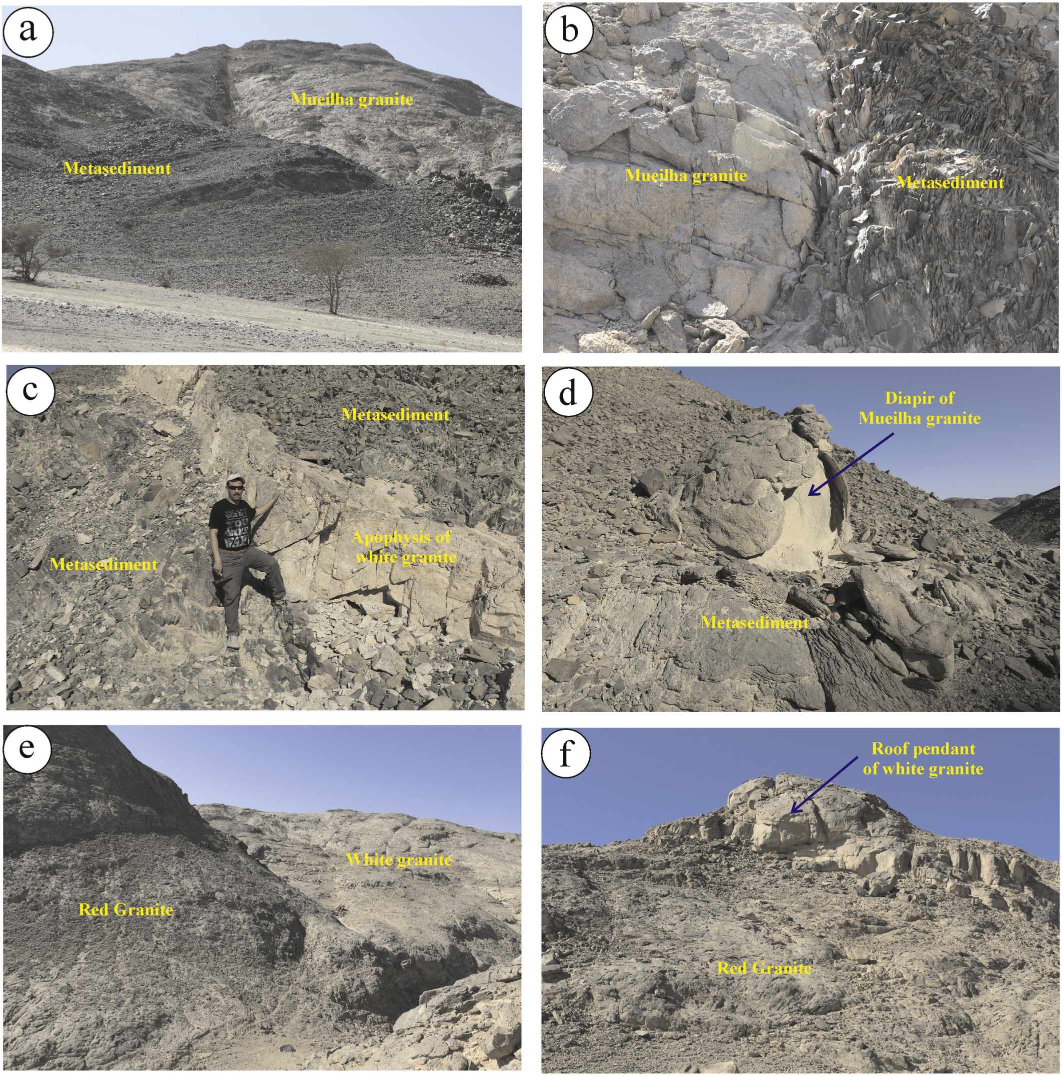
a
Mueilha granite
Metasediment
b
Mueilha granite
Metasediment
c
Metasediment
Metasediment
Apophysis of white granite
d
Diapir of Mueilha granite
Metasediment
e
White granite
Red Granite
f
Roof pendant of white granite
Red Granite

Figure 2

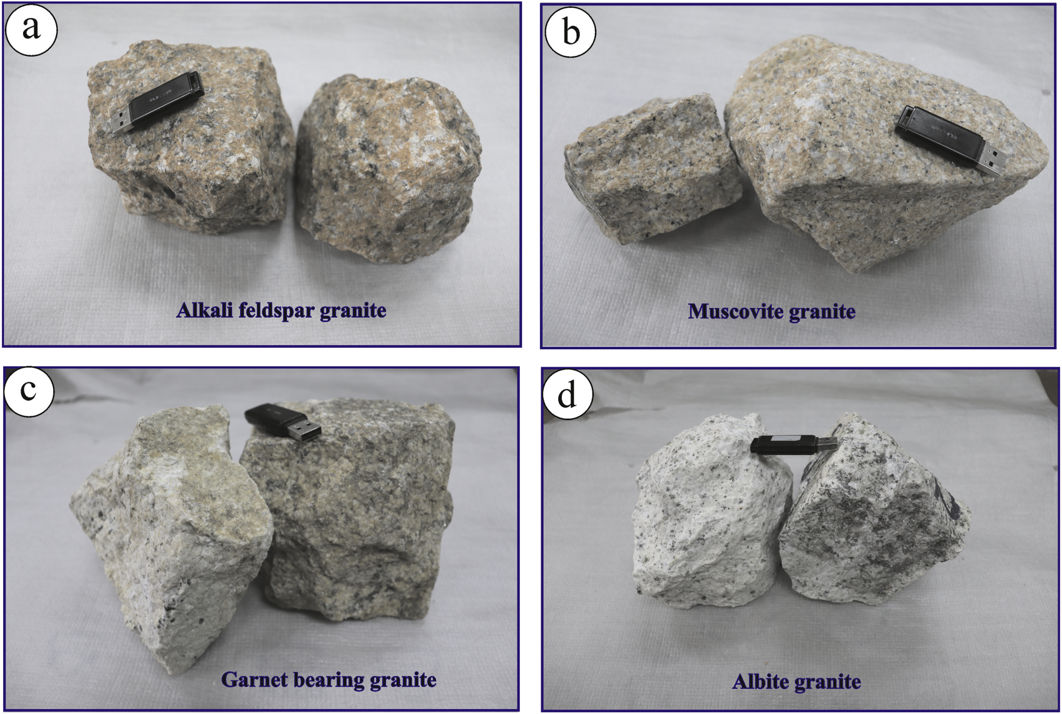
a
Alkali feldspar granite
b
Muscovite granite
c
Garnet bearing granite
d
Albite granite

Figure 3

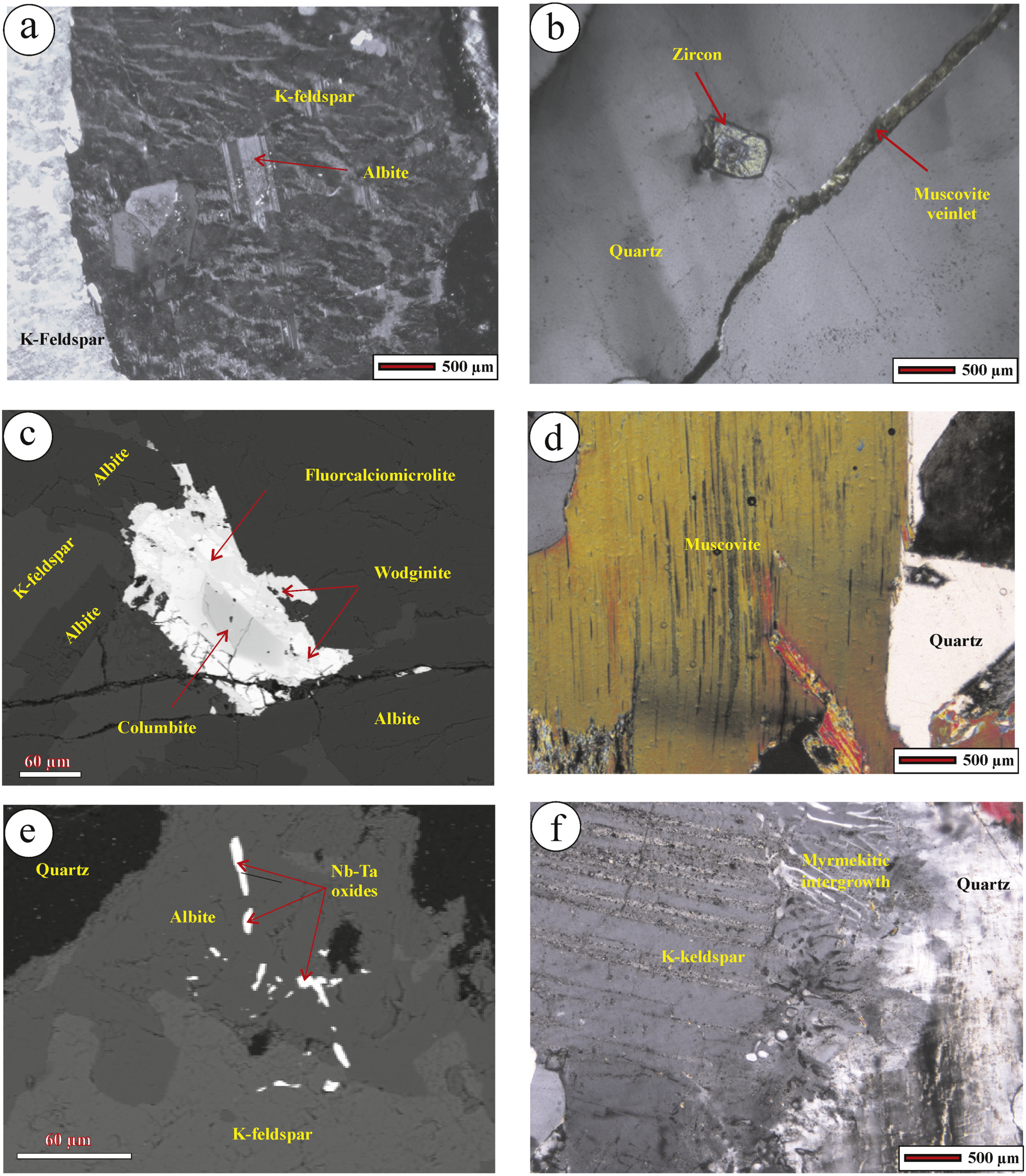
a
K-feldspar
Albite
K-Feldspar
500 µm
b
Zircon
Muscovite veinlet
Quartz
500 µm
c
Albite
Fluorcalciomicrolite
K-feldspar
Wodginite
Albite
Columbite
Albite
60 µm
d
Muscovite
Quartz
500 µm
e
Quartz
Nb-Ta oxides
Albite
60 µm
K-feldspar
f
Myrmekitic intergrowth
Quartz
K-keldspar
500 µm

Figure 4A

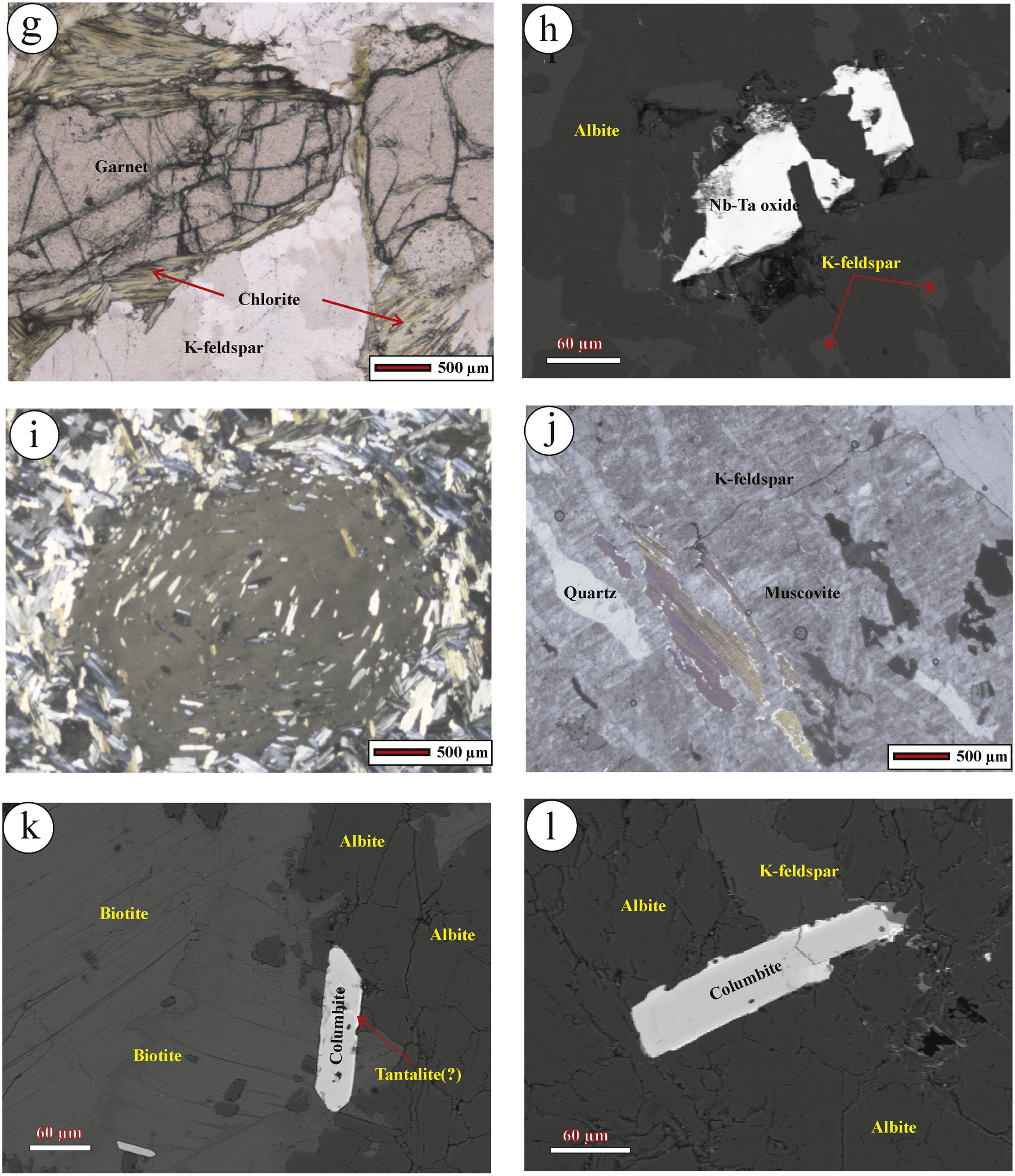
g
Garnet
Chlorite
K-feldspar
500 µm
h
Albite
Nb-Ta oxide
K-feldspar
60 µm
i
500 µm
j
K-feldspar
Quartz
Muscovite
500 µm
k
Albite
Biotite
Albite
Columbite
Biotite
Tantalite(?)
60 µm
l
K-feldspar
Albite
Columbite
Albite
60 µm

Figure 4B

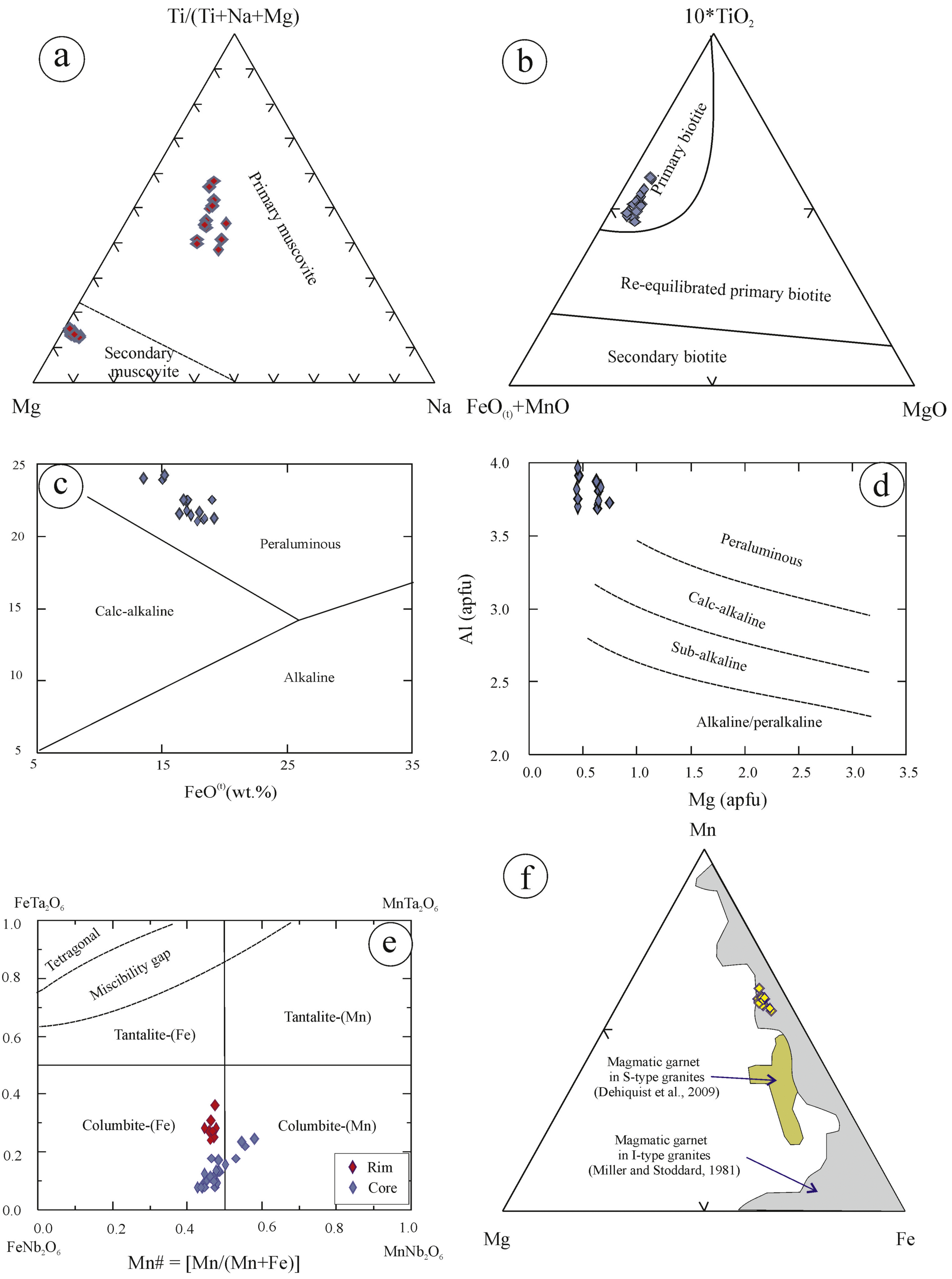
a
Ti/(Ti+Na+Mg)
Primary muscovite
Secondary muscovite
Mg
Na
b
$10*TiO_2$
Primary biotite
Re-equilibrated primary biotite
Secondary biotite
$FeO_{(t)}+MnO$
MgO
c
Al_2O_3 (wt.%)
25
20
15
10
5
Peraluminous
Calc-alkaline
Alkaline
5
15
25
35
$FeO^{(t)}$(wt.%)
d
Al (apfu)
4.0
3.5
3.0
2.5
2.0
Peraluminous
Calc-alkaline
Sub-alkaline
Alkaline/peralkaline
0.0
0.5
1.0
1.5
2.0
2.5
3.0
3.5
Mg (apfu)
e
$FeTa_2O_6$
$MnTa_2O_6$
Ta# = [Ta/(Ta+Nb)]
1.0
0.8
0.6
0.4
0.2
0.0
Tetragonal
Miscibility gap
Tantalite-(Fe)
Tantalite-(Mn)
Columbite-(Fe)
Columbite-(Mn)
Rim
Core
0.0
0.2
0.4
0.6
0.8
1.0
$FeNb_2O_6$
$MnNb_2O_6$
Mn# = [Mn/(Mn+Fe)]
f
Mn
Magmatic garnet in S-type granites (Dehiquist et al., 2009)
Magmatic garnet in I-type granites (Miller and Stoddard, 1981)
Mg
Fe

Figure 5

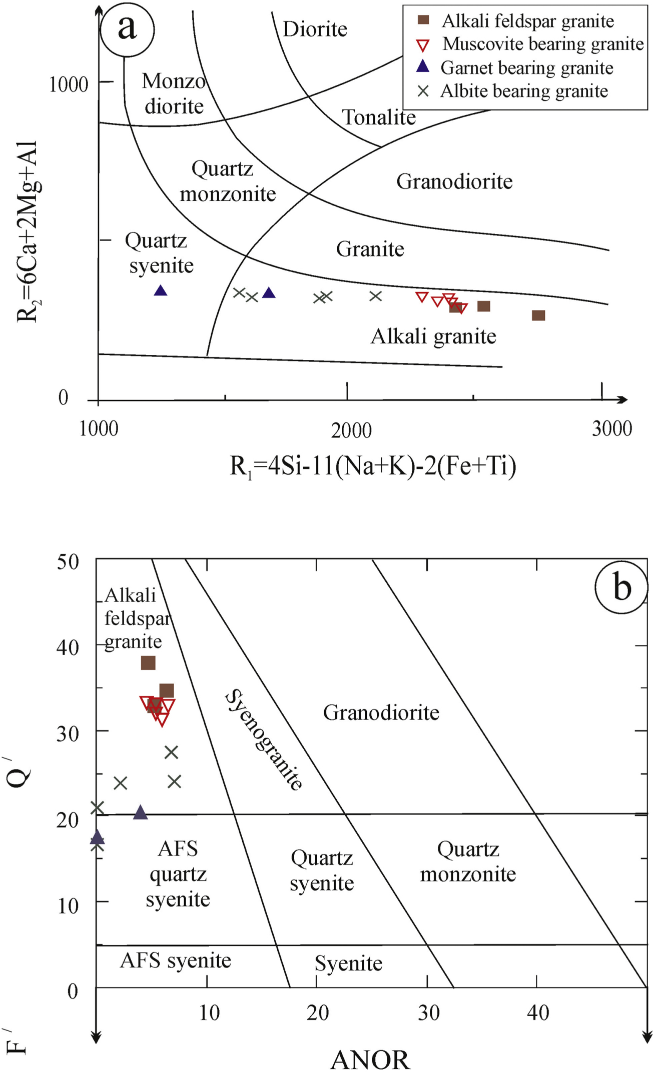
a
Alkali feldspar granite
Muscovite bearing granite
Garnet bearing granite
Albite bearing granite
Diorite
Monzo diorite
Tonalite
Quartz monzonite
Granodiorite
Quartz syenite
Granite
Alkali granite
1000
0
R$_2$=6Ca+2Mg+Al
1000
2000
3000
R$_1$=4Si-11(Na+K)-2(Fe+Ti)
b
50
40
30
20
10
0
Alkali feldspar granite
Syenogranite
Granodiorite
AFS quartz syenite
Quartz syenite
Quartz monzonite
AFS syenite
Syenite
10
20
30
40
Q'
F'
ANOR

Figure 6

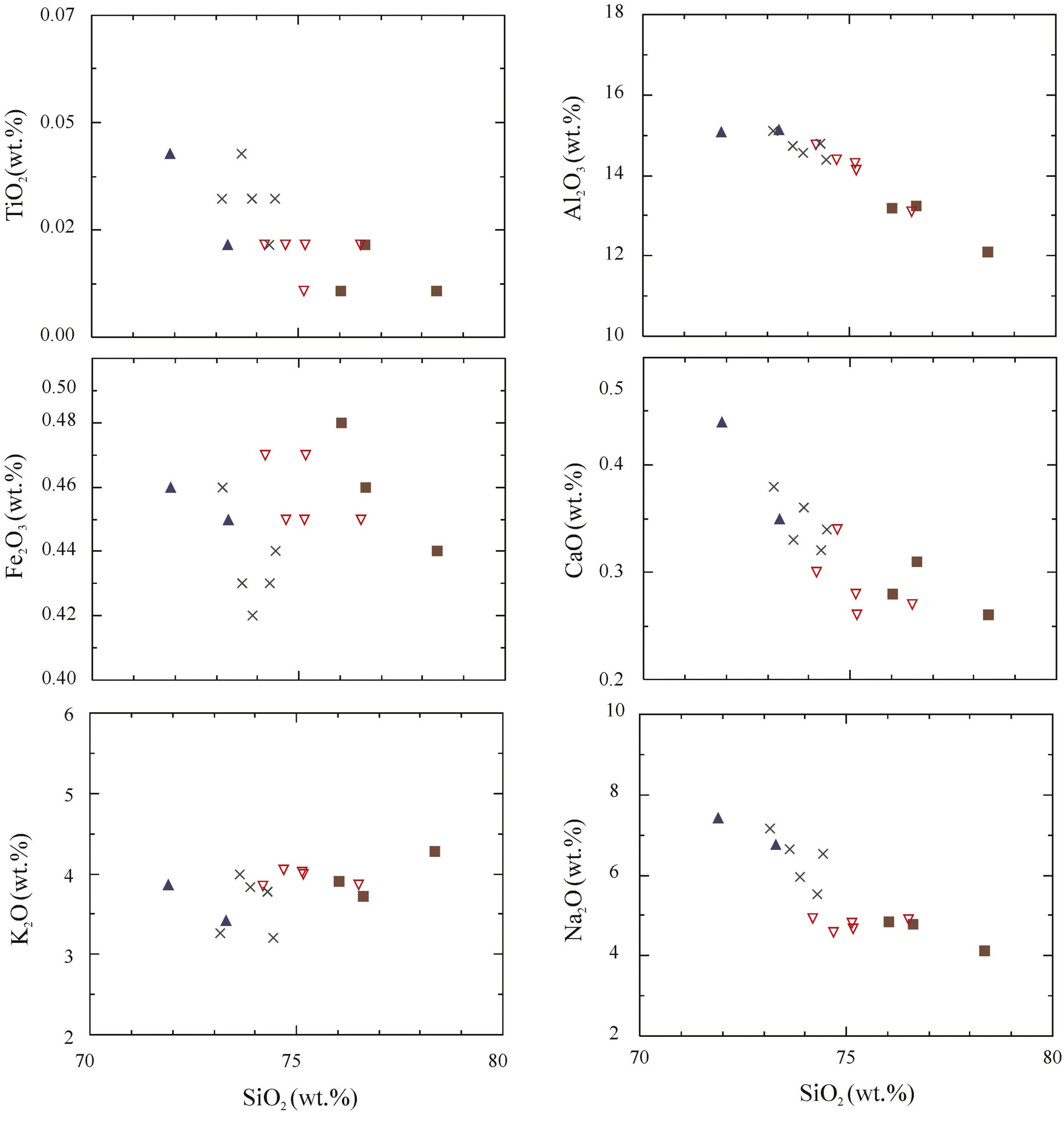

0.07
0.05
0.02
0.00
TiO$_2$(wt.%)
18
16
14
12
10
Al$_2$O$_3$(wt.%)
0.50
0.48
0.46
0.44
0.42
0.40
Fe$_2$O$_3$(wt.%)
0.5
0.4
0.3
0.2
CaO(wt.%)
6
5
4
3
2
K$_2$O(wt.%)
10
8
6
4
2
Na$_2$O(wt.%)
70
75
80
SiO$_2$(wt.%)
70
75
80
SiO$_2$(wt.%)

Figure 7

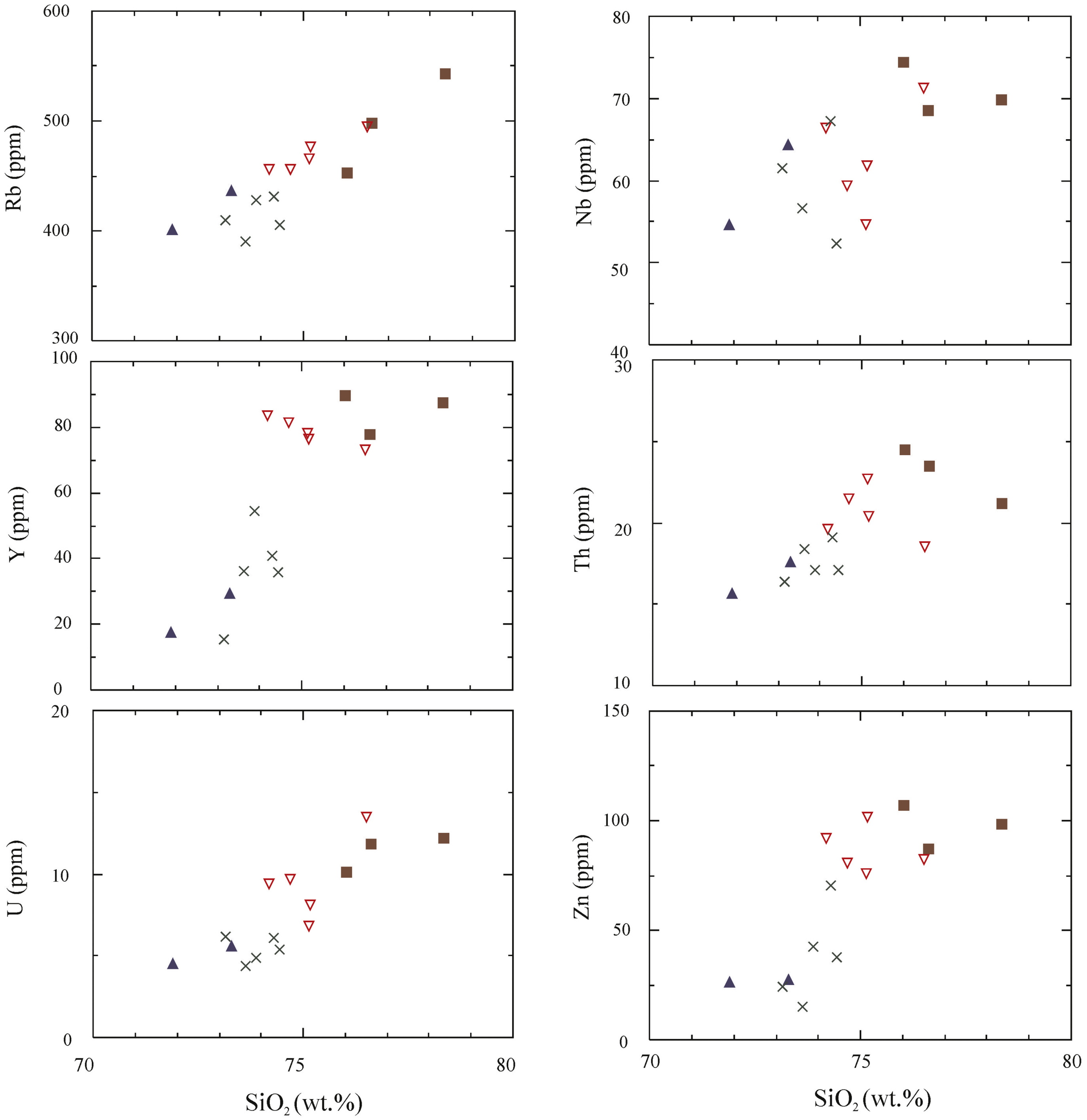
Rb (ppm)
600
500
400
300
Nb (ppm)
80
70
60
50
40
Y (ppm)
100
80
60
40
20
0
Th (ppm)
30
20
10
U (ppm)
20
10
0
Zn (ppm)
150
100
50
0
70
75
80
SiO$_2$ (wt.%)
70
75
80
SiO$_2$ (wt.%)

Figure 8A

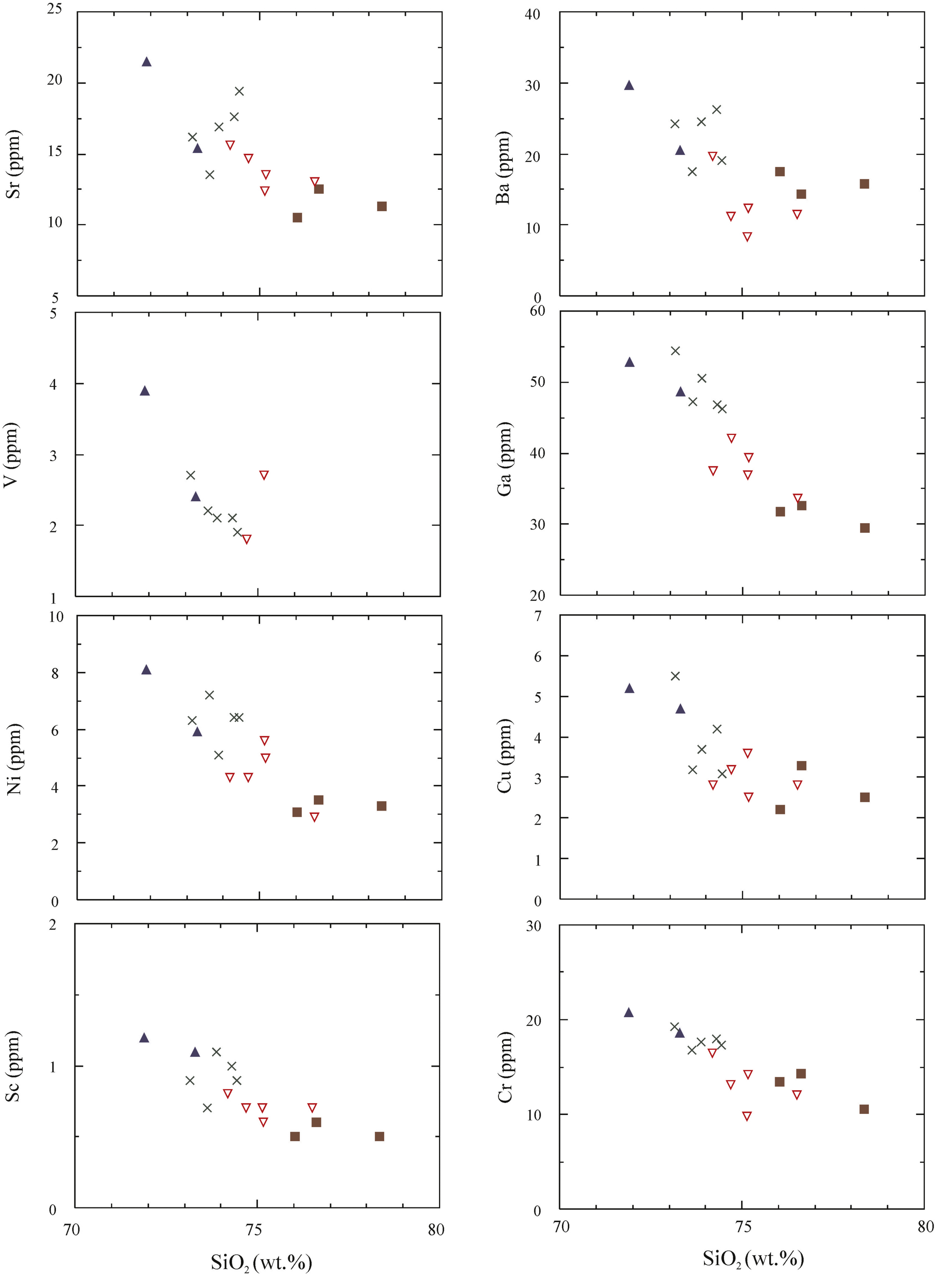

Sr (ppm)
Ba (ppm)
V (ppm)
Ga (ppm)
Ni (ppm)
Cu (ppm)
Sc (ppm)
Cr (ppm)
5
10
15
20
25
0
10
20
30
40
1
2
3
4
5
20
30
40
50
60
0
2
4
6
8
10
0
1
2
3
4
5
6
7
0
1
2
0
10
20
30
70
75
80
SiO$_2$ (wt.%)

Figure 8B

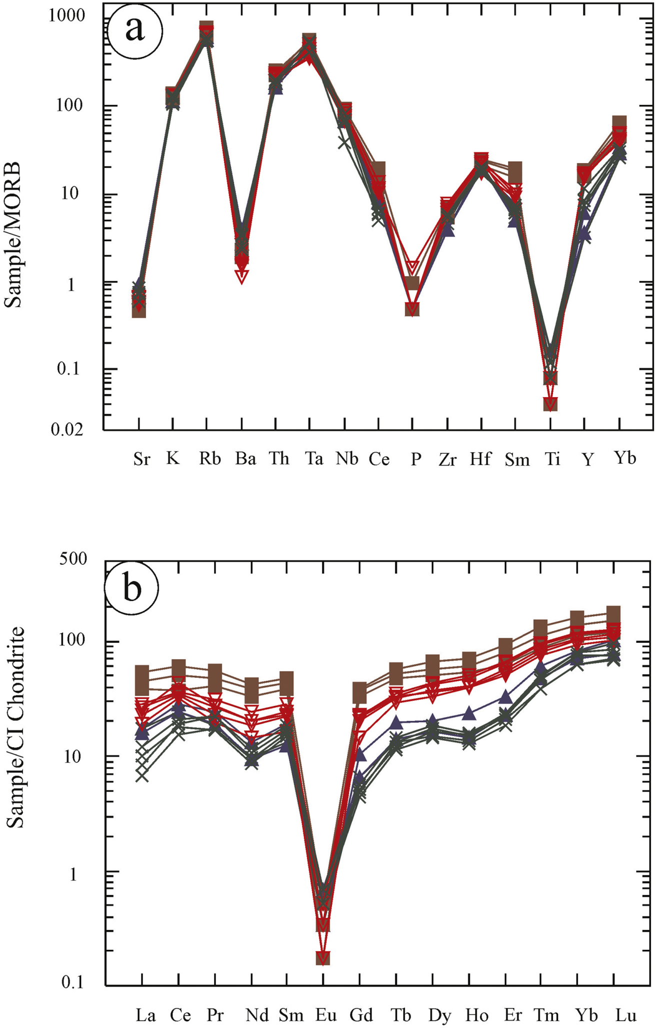
a
Sample/MORB
1000
100
10
1
0.1
0.02
Sr
K
Rb
Ba
Th
Ta
Nb
Ce
P
Zr
Hf
Sm
Ti
Y
Yb
b
Sample/CI Chondrite
500
100
10
1
0.1
La
Ce
Pr
Nd
Sm
Eu
Gd
Tb
Dy
Ho
Er
Tm
Yb
Lu

Figure 9

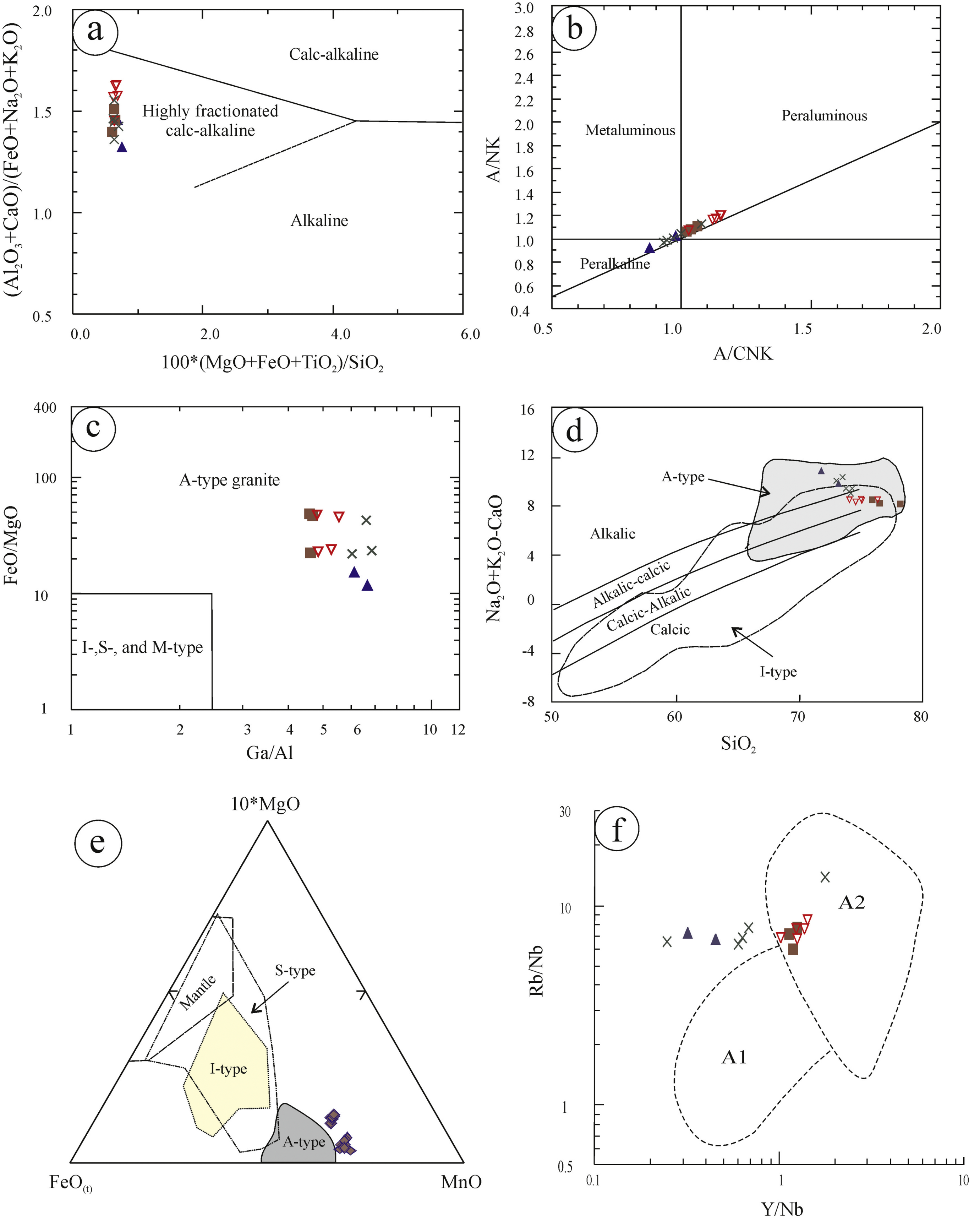
a
Calc-alkaline
Highly fractionated calc-alkaline
Alkaline
$(Al_2O_3+CaO)/(FeO+Na_2O+K_2O)$
$100*(MgO+FeO+TiO_2)/SiO_2$
2.0
1.5
1.0
0.5
0.0
2.0
4.0
6.0
b
Metaluminous
Peraluminous
Peralkaline
A/NK
A/CNK
3.0
2.8
2.6
2.4
2.2
2.0
1.8
1.6
1.4
1.2
1.0
0.8
0.6
0.4
0.5
1.0
1.5
2.0
c
A-type granite
I-,S-, and M-type
FeO/MgO
Ga/Al
400
100
10
1
1
2
3
4
5
6
10
12
d
A-type
Alkalic
Alkalic-calcic
Calcic-Alkalic
Calcic
I-type
Na_2O+K_2O-CaO
SiO_2
16
12
8
4
0
-4
-8
50
60
70
80
e
10*MgO
Mantle
S-type
I-type
A-type
$FeO_{(t)}$
MnO
f
A2
A1
Rb/Nb
Y/Nb
30
10
1
0.5
0.1
1
10

Figure 10

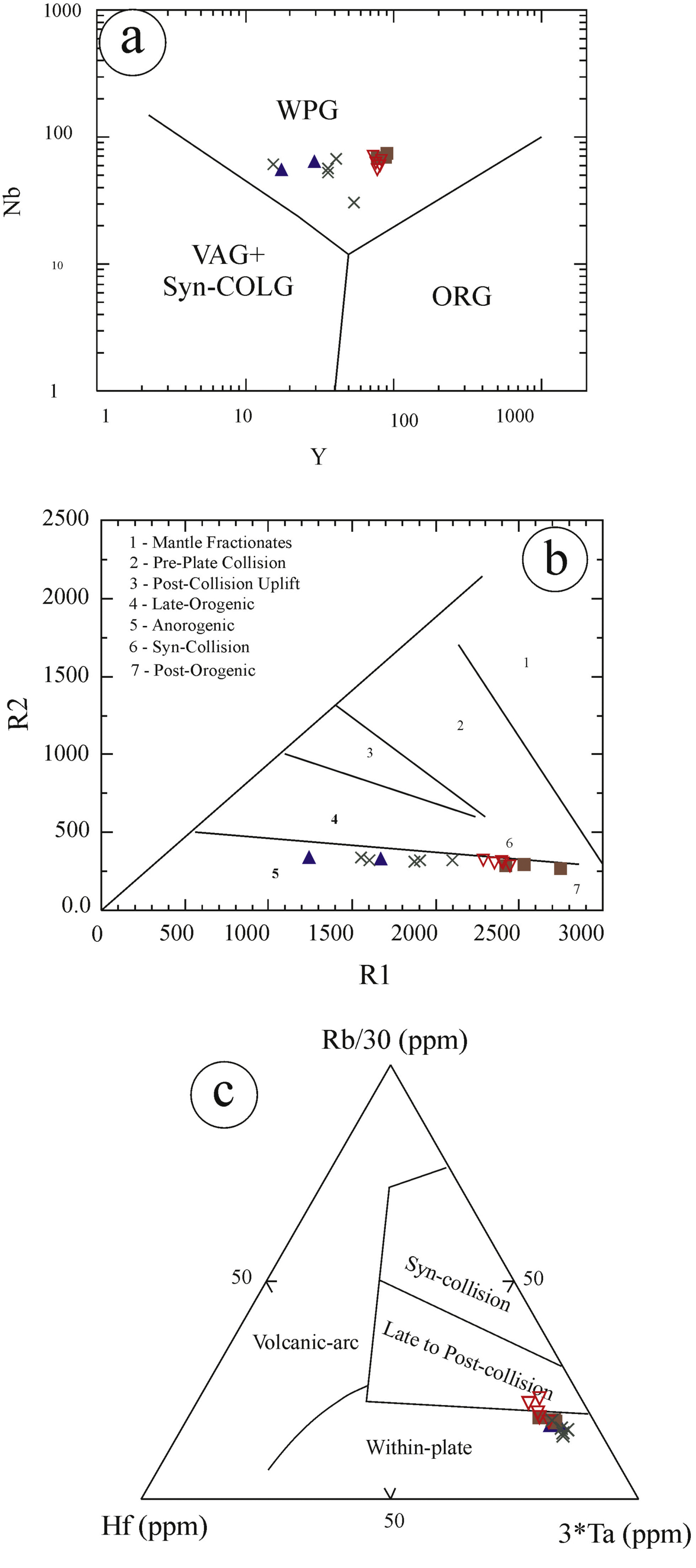
a
1000
100
10
1
Nb
WPG
VAG+
Syn-COLG
ORG
1
10
100
1000
Y
b
2500
2000
1500
1000
500
0.0
R2
0
500
1000
1500
2000
2500
3000
R1
1 - Mantle Fractionates
2 - Pre-Plate Collision
3 - Post-Collision Uplift
4 - Late-Orogenic
5 - Anorogenic
6 - Syn-Collision
7 - Post-Orogenic
1
2
3
4
5
6
7
c
Rb/30 (ppm)
50
50
50
Syn-collision
Volcanic-arc
Late to Post-collision
Within-plate
Hf (ppm)
3*Ta (ppm)

Figure 11

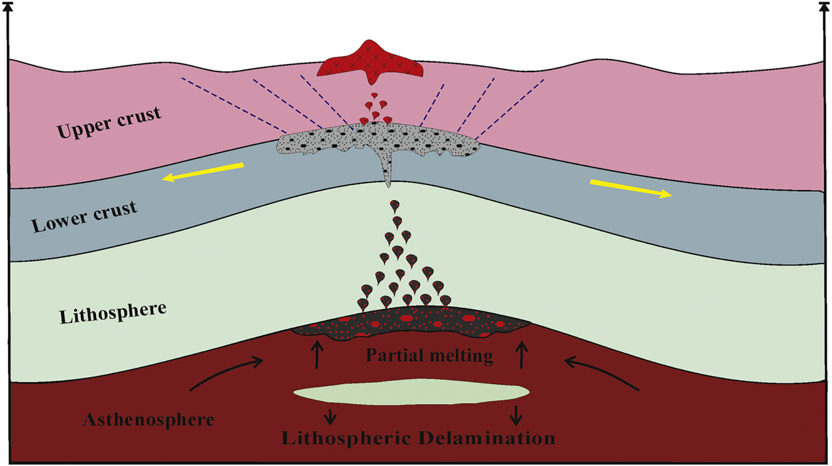
Upper crust
Lower crust
Lithosphere
Partial melting
Asthenosphere
Lithospheric Delamination

Figure 12

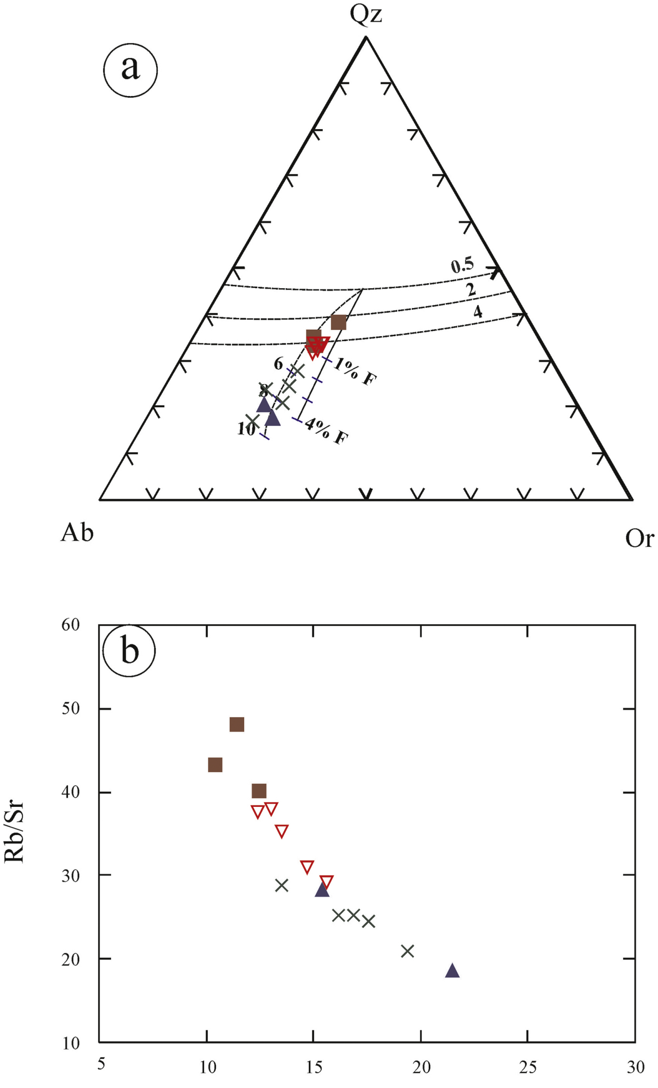

Figure 13